EXPERIMENTAL STUDY OF PIEZOELECTRIC AND DIELECTRIC RESPONSES IN POLY-L-LACTIC ACID

SITI HANNAH BINTI MAT ZIN

FACULTY OF SCIENCE
UNIVERSITI MALAYA
KUALA LUMPUR

2022

EXPERIMENTAL STUDY OF PIEZOELECTRIC AND DIELECTRIC RESPONSES IN POLY-L-LACTIC ACID

SITI HANNAH BINTI MAT ZIN

DISSERTATION SUBMITTED IN FULFILMENT OF THE REQUIREMENTS FOR THE DEGREE OF MASTER OF SCIENCE

DEPARTMENT OF PHYSICS
FACULTY OF SCIENCE
UNIVERSITI MALAYA
KUALA LUMPUR

2022

UNIVERSITI MALAYA

ORIGINAL LITERARY WORK DECLARATION

Name of Candidate: **SITI HANNAH BINTI MAT ZIN**

Matric No: **17028129/2**

Name of Degree: **MASTER OF SCIENCE**

Title of Thesis (“this Work”):

EXPERIMENTAL STUDY OF PIEZOELECTRIC AND DIELECTRIC RESPONSES IN POLY-L-LACTIC ACID

Field of Study:

EXPERIMENTAL PHYSICS

I do solemnly and sincerely declare that:

(1) I am the sole author/writer of this Work;
(2) This Work is original;
(3) Any use of any work in which copyright exists was done by way of fair dealing and for permitted purposes and any excerpt or extract from, or reference to or reproduction of any copyright work has been disclosed expressly and sufficiently and the title of the Work and its authorship have been acknowledged in this Work;
(4) I do not have any actual knowledge nor do I ought reasonably to know that the making of this work constitutes an infringement of any copyright work;
(5) I hereby assign all and every rights in the copyright to this Work to the University of Malaya (“UM”), who henceforth shall be owner of the copyright in this Work and that any reproduction or use in any form or by any means whatsoever is prohibited without the written consent of UM having been first had and obtained;
(6) I am fully aware that if in the course of making this Work I have infringed any copyright whether intentionally or otherwise, I may be subject to legal action or any other action as may be determined by UM.

Candidate’s Signature Date: 31/5/2022

Subscribed and solemnly declared before,

Witness’s Signature Date:31/5/2022

Name:

Designation:

EXPERIMENTAL STUDY OF PIEZOELECTRIC AND DIELECTRIC RESPONSES IN POLY-L-LACTIC ACID

ABSTRACT

The piezoelectric *d*- and *e*-constants, as well as the elastic constant, *c*, and the dielectric constant, ε were determined as a function of frequency and temperature for oriented poly-L-lactic acid (PLLA) films with various elongation ratios and annealing temperatures using the dielectric resonance method. The findings are discussed in terms of a general theory of piezoelectricity for inhomogeneous systems, more specifically a disperse two-phase system. Five observations demonstrate that the piezoelectricity of PLLA film originates from the piezoelectric and optically active symmetry of PLLA crystallites and their orientation distribution. d_{14} component of the piezoelectric matrix is observed. The e_{14} is proportional to the product of orientation factor, F_c and crystallization fraction, X_c ($F_c * X_c$) of PLLA crystallites as determined by x-ray diffraction. The piezoelectric constants for a perfect crystal of PLLA was determined as e_{14} ~27 mC/m^2 from the three-spring model and extrapolation to perfect orientation using the correlation of $F_c * X_c$ assuming the PLLA crystallites are rigid. At ~100°C, the piezoelectric relaxation of PLLA is due to segmental mode relaxation in the amorphous phase within the crystalline region. A significant decrease in e_{14} with increasing temperature is caused by the non-crystalline phase softening, which results in a decrease in strain in the crystalline phase. The retardation of d_{14} is due to softening in the non-crystalline region caused by a parallel crystalline phase's stress concentration. An equivalent model is proposed that incorporates the PLLA film's higher order structure.

.

Keywords: piezoelectric, dielectric, polylactic acid, biopolymer, resonance

KAJIAN EKSPERIMEN TINDAK BALAS PIEZOELEKTRIK DAN DIELEKTRIK DALAM POLI-L-LAKTIK ASID

ABSTRAK

Pemalar piezoelektrik *d*-dan *e*, serta pemalar elastik, *c*, dan pemalar dielektrik, ε ditentukan sebagai fungsi frekuensi dan suhu untuk sampel poli-L-laktik asid (PLLA) berorientasi dengan pelbagai nisbah pemanjangan dan suhu penyepuhlindapan menggunakan kaedah resonans dielektrik. Penemuan ini dibincangkan dari segi teori umum piezoelektrik untuk sistem tidak homogen, lebih khusus lagi bagi sistem dua fasa tersebar. Lima pemerhatian menunjukkan bahawa piezoelektrik bagi sampel PLLA berasal dari simetri piezoelektrik dan optik aktif kristal PLLA dan taburan orientasinya. Komponen matriks piezoelektrik d_{14} diperhatikan. e_{14} berkadar langsung dengan tahap orientasi $F_c{*}X_c$ kristal PLLA seperti yang ditentukan oleh difraksi sinar-X. Pemalar piezoelektrik bagi kristal sempurna untuk PLLA ditentukan sebagai $e_{14} \sim 27$ mC / m^2 dari model tiga spring dan ekstrapolasi ke orientasi sempurna menggunakan korelasi $F_c * X_c$ dengan anggapan kristal PLLA padat. Pada suhu ~ 100 ° C, relaksasi piezoelektrik PLLA disebabkan oleh relaksasi mod segmental dalam fasa amorf dalam kawasan kristal. Penurunan yang ketara pada e_{14} dengan peningkatan suhu disebabkan oleh pelembutan fasa non-kristal, yang mengakibatkan penurunan ketegangan pada fasa kristal. Penundaan d_{14} disebabkan oleh pelembutan di kawasan bukan kristal yang disebabkan oleh kepekatan tekanan fasa kristal selari. Model setara dicadangkan yang menggabungkan struktur tersusun tinggi filem PLLA

Kata kunci: piezoelektrik, dielektrik, polilaktikasid, biopolimer, resonans

ACKNOWLEDGEMENTS

First of all, I thank Allah the Almighty for all His providence in carrying out this work successfully.

I would like to express my deepest gratitude to my supervisor, Dr Thamil Selvi Velayutham for her guidance, support, patience and encouragement throughout the course of the work. I would also like to thank Professor Takeo Furukawa for research guidance and invaluable discussion on the topic of shear piezoelectricity.

I am grateful for the attentions and support from my beloved family. I am indebted to my late father Mat Zin Bin Kasim and my late mother Isbah Binti L.Muhamad for their encouragement throughout the years of my life. Hereby, I placed on record to dedicate this thesis to my beloved parents.

Also, I'd like to express my heartfelt gratitude to my lab mates for their moral support during the difficult times we faced while working together.

Last but not least, I want to express my gratitude to everyone who has helped me to complete my research, whether directly or indirectly.

TABLE OF CONTENTS

ABSTRACT .... **iii**

ABSTRAK .... **iv**

ACKNOWLEDGEMENTS .... **v**

TABLE OF CONTENTS .... **vi**

LIST OF FIGURES. .... **ix**

LIST OF TABLES .... **xii**

LIST OF SYMBOLS AND ABBREVIATIONS .... **xiii**

LIST OF APPENDICES .... **xv**

CHAPTER 1: INTRODUCTION **16**

1.1 History of Piezoelectricity and Applications 16

1.2 Piezoelectricity in polymers 17

1.3 Poly-L-lactic acid (PLLA) 18

  1.3.1 Applications of PLLA 19

1.4 Problem Statements and Objectives 21

1.5 Thesis structure 22

CHAPTER 2: LITERATURE REVIEW **24**

2.1 Introduction 24

2.2 Dielectrics 24

2.3 Piezoelectricity 30

2.4 Piezoelectric polymers 34

2.5 Poly-l-lactic acid (PLLA) 35

  2.5.1 Synthesis of PLLA 35

  2.5.2 Chain conformations and crystal structures 37

2.5.3 Effect of crystallinity on dielectric relaxations 37
2.5.4 Piezoelectricity of PLLA and resonance measurements 40
2.5.5 Basic Analysis of drawn chiral polymers' piezoelectric resonance 44
2.5.6 Effect of crystallinity and orientation on piezoelectricity of PLLA 49

CHAPTER 3: METHODOLOGY 51

3.1 Overview 51
3.2 PLLA film preparation 51
3.2.1 Uniaxial expansion of the PLLA film 51
3.3 Cutting the PLLA film 53
3.4 Characterization 54
3.4.1 Differential Scanning Calorimetry (DSC) 54
3.4.2 Wide Angle X-Ray Scattering (WAXS) 56
3.5 Electrical Measurements 59
3.5.1 Dielectric & piezoelectric measurements 59

CHAPTER 4: RESULTS AND DISCUSSION 62

4.1 Introduction 62
4.2 Wide Angle X-ray Scattering (WAXS) 62
4.2.1 Non-drawn PLLA films 62
4.2.2 Uniaxially drawn PLLA films 64
4.3 Differential Scanning Calorimetry (DSC) 70
4.4 Dielectric relaxation spectroscopy 73
4.5 Piezoelectric relaxation 80
4.6 The effect of crystallinity and chain orientation on the piezoelectric constants of PLLA 87
4.7 Summary 91

CHAPTER 5: CONCLUSIONS 93

REFERENCES 96

LIST OF PUBLICATIONS AND PAPERS PRESENTED 102

APPENDIX 103

LIST OF FIGURES.

Figure 2.1 : Illustration of three types of polarization…………………… 26

Figure 2.2 : Linear electromechanical equations…………………………… 30

Figure 2.3 : Macroscopic piezoelectric effect………………………………. 31

Figure 2.4 : Mechanical and piezoelectric stress examples in the four possible orientations…………………………………………… 34

Figure 2.5 : Stereoisomers of lactic acid……………………………………. 36

Figure 2.6 : Polymerization reaction of lactic acid…………………………. 36

Figure 2.7 : (a) Evolution of dielectric strength of three relaxations in PLLA during the crystallization and (b) the AFM image during crystallization at 150°C after 35 minutes…………………… 38

Figure 2.8 : Isothermal dielectric loss spectra of semicrystalline PLLA for α relaxation from 60°C to 100°C with different crystallization temperature, T_{c}. Inset presents the temperature dependence of dielectric strength, $\Delta\varepsilon$……………………………………….. 39

Figure 2.9 : Average relaxation time as a function of reciprocal temperature for wholly amorphous (open circle) and crystalline (solid circle) PLLA…………………………………………….. 40

Figure 2.10 : Schematic diagram of macro symmetry in PLLA due to mechanical drawing……………………………………........... 41

Figure 2.11 : a) Length extension (LE) and width extension (WE) mode (b) thickness extension (TE) mode………………………………... 42

Figure 2.12 : The observed (red circle) and fitted (blue line) curve of dielectric permittivity (sample dimension: 20 mm x 7 mm x 40 µm)……………………………………………………… 42

Figure 2.13 : Cartesian coordinate systems assigned to uniaxially oriented films (*x,y,z*) and 45° cut for square sample (*x′,y′,z′*)…………… 44

Figure 2.14 : Shear piezoelectricity (measured at 44.2 °C and 20 Hz) of polylactic acid versus the product of crystallinity*orientation (X_{c}*F_{c})……………………………………………………..... 50

Figure 3.1 : The PLLA film before and after drawing at ratio 5………….. 52

Figure 3.2 : The drawing process…………………………………………… 53

Figure 3.3 : The 45° cutting angle of the elongated PLLA film…………. 53

Figure 3.4 : The illustration of DSC………………………………………... 54

Figure 3.5 : The DSC curve for poly(ethylene terephthalate), PET………... 55

Figure 3.6 : The WAXS setup at Beamline 1.3 SLRI…………………… 56

Figure 3.7 : Cartesian coordinate systems utilized to characterize a crystallite's orientation. The *Z*-axis is the film's orientation direction, while the Z^c-axis is the crystallite's orientation axis (the *c*-axis). (b) The technique of symmetrical transmission is used to measure $\boldsymbol{I\chi}$…………………………………………….. 58

Figure 3.8 : (a) The dielectric measurement setup and (b) the setup of the sample inside the cryostat…………………………………… 60

Figure 4.1 : (a) 2D WAXS image and (b) 1D WAXS profile for nondrawn sample annealed from 80 °C to 160 °C……………………... 63

Figure 4.2 : (a) The plot illustrates deconvolution of the WAXS plot in the PLLA film (non- drawn and annealed). (b) The plot displays the evaluated percentage of crystallinity, X_c of the neat (non-drawn and non-annealed) and non-drawn film annealed at 80 °C, 100 °C, 120 °C, 140 °C and 160 °C……………………….. 64

Figure 4.3 : (a) 2D WAXS images for various drawing ratio samples annealed at 160°C, (b) 1D WAXS profile for λ=2 annealed at different temperature, (c) 1D WAXS profile for different drawing ratio sample annealed at 160 °C…………………… 66

Figure 4.4 : X-ray diffraction patterns and their crystalline and amorphous peak deconvolution curves for samples (a) λ=2; T_a = 80 °C, (b) λ=2; T_a = 160 °C, (c) λ=6; T_a =80 °C, (d) λ=6; T_a =160 °C. Fig 4.4 (e) shows the degree of crystallinity, X_c versus annealing temperatures for various drawing ratios……………………….. 68

Figure 4.5 : Changes of F_c as a function of annealing temperature and drawing ratio……………………………………………........... 69

Figure 4.6 : Deformation model for crystallites and amorphous region during uniaxial drawing………………………………….......... 70

Figure 4.7 : DSC thermograms plot of the samples (a) annealed at various temperatures and (b) uniaxially drawn at various drawing ratios and annealed at 160 °C………………………………….. 73

Figure 4.8 : Complex permittivity of PLLA heating from 25 °C to 140 °C with a temperature step of 5 °C for (a) neat film (amorphous sample) (b) uniaxially drawn, λ =6 and annealed at 160 °C (highly oriented and crystalline sample)……………………… 74

Figure 4.9 : The exemplary fitting of the piezo resonance and dielectric relaxation of PLLA measured at 90 °C……………………... 76

Figure 4.10 : (a) Dielectric strength as a function of temperature for α- and β-relaxation. (b) Arrhenius plots for the α- and β-relaxation……………………………………………………. 78

Figure 4.11 : Temperature dependence of the (a) coupling coefficient, k, compliance, s and the dielectric modulus, ε at 100 kHz for the oriented PLLA film. and the (b) piezoelectric constant d_{14} and e_{14} and elastic constant, c……………………………………… 81

Figure 4.12 : The changes in the resonance peaks as the temperature increased from 40 °C to 100 °C is illustrated in the figure……. 82

Figure 4.13 : Three-spring model consisting of piezoelectric crystalline spring G_2 surrounded by noncrystalline relaxational springs connected in series G_1 and parallel G_3 to G_1…………………... 83

Figure 4.14 : (a) The calculated G complex from three element model with the c_{44} and (b) the calculated L_s and L_T……………………... 85

Figure 4.15 : The observed experimental results of (a) c_{44}, (b) e_{14} and (c) d_{14} were fitted using a three-element model (the experimental points are the red circles while the fitted curves are the blue lines)………………………………………………………. 86

Figure 4.16 : Crystallinity, X_c as a function of the orientation, F_c for PLLA films……………………………………………………………. 87

Figure 4.17 : Dependence of (a) e_{14} and d_{14} and the (b) c_{44} on the product of X_c*F_c of PLLA samples at room temperature, respectively…………………………………………………….. 88

LIST OF TABLES

Table 2.1 : Comparison of the piezoelectric constants of three optically active polymers. 35

Table 4.1 : The glass transition temperature (T_g), melting temperature (T_m), enthalpy of cold crystallization (ΔH_c) and enthalpy of melting (ΔH_f) of the non-drawn sample measured at different annealing temperatures. 71

Table 4.2 : The glass transition temperature (T_g), melting temperature (T_m), enthalpy of cold crystallization (ΔH_c) and enthalpy of melting (ΔH_f) of the PLLA samples drawn at various ratios and annealed at 160 °C. 72

Table 4.3 : Parameters of the VFT and Arrhenius equation 79

LIST OF SYMBOLS AND ABBREVIATIONS

E_A : Activation energy

ω : Angular frequency

C_p : Capacitance

ΔH_c : Cold crystallization heat

ε^* : Complex permittivity

T_c : Crystallization temperature

λ : Drawing ratio

ρ : Density

$\tan\delta$: Dissipation factor

$\Delta\varepsilon$: Dielectric strength

s_{jl} : Elastic compliance

c_{jl} : Elastic constant

D : Electric displacement

E : Electric field

χ_e : Electric susceptibility

k : Electromechanical coupling factor

F : Force

T_g : Glass transition temperature

ε'' : Imaginary permittivity

ε_∞ : Infinitive relative dielectric

P_2 : Legendre polynomial

E_{loc} : Local electric field

L_F : Local force normalized by applied force

$L_{\Delta l}$: Local deformation normalized by applied deformation

ΔH_m : Melting heat

T_m : Melting temperature

F_c : Orientation factor

X_c : Percentage of crystallinity

d_{14} : Piezoelectric constant

e_{14} : Piezoelectric constant

P : Polarization of dielectric material

f : Resonance frequency

ε' : Real permittivity

τ : Relaxation time

I : Scattering intensity

ε_S : Static dielectric permittivity

S : strain

T : stress

ε_o : Vacuum permittivity

$\emptyset$: Volume fraction of crystallites

T_0 : Vogel temperature

MAP : Mobile amorphous phase

PLLA : Poly-L-lactic acid

PDLA : Poly-D-lactic acid

PVDF : Poly(vinylidene fluoride)

RAP : Rigid amorphous phase

ROP : Ring-open polymerizing

VFT : Vogel-Fulcher-Tammann

LIST OF APPENDICES

Appendix A : The 1D-WAXS profile for different drawing ratios and annealing temperatures ………………………………. 103

Appendix B : 2D WAXS image of (a) PLLA film drawn at λ=2 annealed at different temperature and (b) PLLA film drawn at different ratio with constant T_a=160 °C ………………………………………………………….. 104

Appendix C : The evolution of halo amorphous peak (green dashed line) as the drawing ratio is varied at a constant annealing temperature…………………………………………….. 105

CHAPTER 1: INTRODUCTION

1.1 History of Piezoelectricity and Applications

Pierre Curie's prior research on the relationship between pyroelectric activities and crystal symmetries led the two brothers to explore for pressure-induced electrification and predict its direction and effect on different classes of crystals. These include zinc blende, sodium chlorite, boracite, tourmaline (quartz), topaz, tartaric acid, cane sugar, and Rochelle salt. The findings were published in March 1880 in the French scientific journal Cornptes Rendus (Curie & Curie). It is referred to as the direct piezoelectric effect. On the other hand, the converse piezoelectric effect, defined as the change in the size of the crystal due to the application of a voltage, was predicted theoretically by Lippman and confirmed the following year by the Curies. Although the Curies discovered some of the relationships between piezoelectricity and crystal structure, Woldemar Voigt thoroughly established them in 1894. By combining the symmetry elements of elastic tensors and electric vectors with the geometrical symmetry elements of crystals, he demonstrated that piezoelectric effects can exist in 20 of the 32 crystal classes and that each of the possible 18 piezoelectric coefficients can have a value other than zero (Arnau & Soares, 2008).

The application on piezoelectricity gained popularity throughout the two world wars. In World War I, sonar was the first significant application of piezoelectricity. It was invented in 1917 in France by physicist Paul Langevin and his colleagues. A quartz crystal was a critical component of the sonar's transducer, which was used to detect submarines (Katzir, 2012). During World War II, the discovery of ferroelectrics and the creation of barium titanate, and later lead zirconate titanate (PZT), increased the popularity and need for higher performing piezoelectric ceramics. However, following the war, the United States struggled to extend its market further due to their corporations' extensive use of secrecy and patents. However, in Japan, the businesses collaborated on the creation of piezoelectric materials and quickly commercialized them by developing piezoelectric filters for electronic goods such as televisions and radios (Uchino, 2017). The topic of piezoelectricity will be covered in detail in Chapter 2, including some theoretical equations.

1.2 Piezoelectricity in polymers

Piezoelectricity in polymers was discovered by Kawai et al. (2007) especially in poly(vinylidene fluoride) (PVDF) in the year of 1969. PVDF is the most commonly documented piezoelectric polymer and the best all-around electroactive polymer up to this point (Ounaies et al. 1999). The piezoelectric properties in polymers are related to the polymer's molecular structure (monomer properties and chain conformation) and orientation. The primary disadvantage of piezoelectric polymers is that they have lower piezoelectric coefficients (d_{33}~30 pC/N) (Bauer & Bauer, 2008) than other piezoelectric materials. Their piezoelectric stress constant, on the other hand, is significantly larger, indicating that they are well suited for use as sensors. Additional significant advantages of polymers include their inexpensive production costs, light weight (low density), and excellent flexibility. Additionally, they have a strong dielectric breakdown and a low dielectric constant.

Semicrystalline (which constitute the majority of piezoelectric polymers) and amorphous polymers are the two main types of piezoelectric polymers. Semicrystalline piezoelectric polymers exhibit a polar crystalline phase. Mechanical orientation, thermal annealing, or high voltage (poling) treatment are all suitable methods for introducing the piezoelectricity in the crystalline phase in the polymer. A non-crystalline polymer can exhibit the piezoelectric effect if its molecular structure contains large molecular dipoles.

Generally, amorphous piezoelectric polymers have a weaker piezoelectric response than semicrystalline polymers.

Many researchers have recently become interested in piezoelectricity in biopolymers since it has a lot of potential in biomedical applications. Some of the examples are collagen, polypeptides like poly(γ-methylglutamate) and poly(γ-benzyl-L-glutamate), oriented films of DNA, poly(lactic) acid's family and chitin (Fukada, 1995). The piezoelectric constant of biopolymers is lower than that of conventional synthetic polymers. The internal rotation of polar atomic groups linked to the asymmetrical carbon atoms is the source of piezoelectricity in biopolymers. Poly-L-lactic acid (PLLA), which was elongated four times, had the highest piezoelectric constant (~10pC/N) at room temperature among the well-known chiral bio-polymers (Fukada, 1995).

1.3 Poly-L-lactic acid (PLLA)

Poly-L-lactic acid (PLLA) is a biodegradable semicrystalline thermoplastic polymer. It is a transparent and very flexible plant-derived polymeric material. It is biocompatible and degrades via a hydrolysis reaction that produces lactic acid (LA). Since LA is destroyed in the body's carbohydrate cycle, PLLA and its copolymers are particularly well suited for usage in biomedical applications as sutures and bone fixation devices in the form of pins, rods, plates, and screws. Additionally, these materials can be used as medication delivery vehicles, scaffolds for cell culture, and commodity packaging materials (Guerin et al., (2019); Shin et al., (2020); Tajitsu, 2008).

PLLA crystallizes into at least three polymorphs (α-, β-, and γ-) depending on the preparation condition. De Santis & Kovacs (1968) were the first to report the structure of the α-form and postulated a pseudo-orthorhombic structure (a = 10.6 Å, b = 6.1 Å and c = 28.8 Å) with two chains flowing through the unit cell, each in a left-handed 10/3 configuration (Kobayashi et al., (1995); Montes de Oca & Ward, 2007). Eling et al. (1982)

discovered the second polymorph, termed the β-structure, in the early 1980s. Hoogsteen et al. (1990) revealed the Cartesian coordinates of the atoms in the repetition unit of the α and β structures in 1990, but the difficulty of resolving the chains' relative positions inside the cell remained unsolved. Kobayashi et al. (1995) disclosed the relative placements of the two monomeric residues within the α- form's cell five years later. The orthorhombic unit cell of β-structure is (a = 10.31 Å, b = 18.21 Å and c = 9.00 Å) containing six chains was proposed by Hoogsteen et al. (1990). The chain conformation of β-form PLLA is left-handed 3/1 helices. The third crystal modification of PLLA, or the γ form, appears during epitaxial crystallization on a hexamethylbenzene substrate. It was reported to have two antiparallel helices packed in an orthorhombic unit cell with dimensions of a =9.95 Å, b =6.25 Å, and c= 8.8 Å (L. Cartier et al., 2000). The transformation from α- to β-form occurs when PLLA is oriented at high temperatures and strain rates.

The physical properties of PLLA naturally depend on its crystallinity. Control of the degree of crystallinity is important as a guiding principle for the development of PLLA for practical applications. Despite its intricate higher-ordered structure with intermingled crystalline and amorphous regions, the degree of crystallinity of PLLA can be controlled via a thermal annealing method. By enhancing crystallinity and molecular orientation, the piezoelectric constant of a PLLA film can be tailored and improved (Fukada, 1998; Yoshida et al., 2010).

1.3.1 Applications of PLLA

Due to the high cost and scarcity of PLA, its use was initially limited to medical applications. However, high M_w PLA can now be processed by injection molding, sheet and film extrusion, blow molding, foaming, fiber spinning, and thermoforming. Additionally, when compared to widely accessible commodity polymers such as polypropylene (PP), poly(ethylene terephthalate) (PET), and polystyrene (PS), PLA exhibits comparable optical, mechanical, thermal, and barrier properties, hence broadening its commercial range of uses (Auras., et al (2004); Jie Ren, 2011; Rudnik, 2008; Vink & Davies, 2015).PLA is widely employed in the medical area due to its biocompatibility with the human body, including medical implants, surgical sutures, and medical gadgets.

Furthermore, PLA has been used in fibres, textiles, plastic culture, service ware, packing containers (i.e., food packaging for short-life items), and environmental remediation films. The US Food and Drug Administration (FDA) considers PLA to be a Generally Recognized as Safe (GRAS) substance (Ahmed & Varshney, 2011).

PLA, on the other hand, has some limitations (e.g., poor toughness), so research efforts are focused on obtaining PLA products with specific desired properties by blending PLA with other biodegradable and non-biodegradable resins, and/or by compounding PLA with fillers such as fibres or micro- and nanoparticles.

PLLA films, are expected to be used as sensors and actuators in unconventional Human Machine Interface (HMIs) due to their high flexibility and transparency. A PLLA sensor was combined with a projected capacitive touch panel to realize a deformation-sensitive touch panel. This sensor has been developed by world-famous electronic device company, Murata Manufacturing Co., Ltd (Ando et al., 2012). In addition, they have reported a new sensing technique using a shear piezoelectric PLLA fiber and demonstrated a soft sensor using left- and right-wound PLLA fibers. Based on these fundamental results, they attempted to develop a piezoelectric PLLA fabric fabricated by drawing piezoelectric PLLA fibers (Tajitsu, 2008, 2010; Tajitsu et al., 2004). They reported a prototype system that detects simple movements of a human wearing clothes made of piezoelectric PLLA fabric, i.e., the extension of an arm, the bending of an elbow, and the twisting of a wrist, through the motion detection of the piezoelectric PLLA fabric; these movements were linked to those of a humanoid robot (Tajitsu, 2016).

1.4 Problem Statements and Objectives

Previously, several research studies have been conducted to evaluate the influence of crystallization and stereochemistry on PLLA dynamics (Ana Rita Brás et al., (2006); Mijović & Sy, 2002). However, in-depth research on the piezoelectric characteristics of PLLA is hardly reported. Theory and experiment have revealed that the shear piezoelectricity of polymers is proportional to the crystalline content (X_c) and orientation factor (F_c) of the polymer (Takeo Furukawa & Fukada, 1976). The linear link between shear piezoelectricity and the X_c*F_c product is well established in this research, but none of them attempted to manipulate these parameters independently in a wider range of X_c or F_c or to determine the influence of each parameter separately. Due to its well-known shear piezoelectric characteristics and adjustable crystallinity, PLLA was chosen for this experiment to facilitate decoupling of crystallinity and orientation. Drawing the PLLA samples to higher drawing ratios is a challenge task because of its brittle nature at room temperature. In this study we attempted to uniaxially draw the PLLA film to higher drawing ratios at elevated temperature in a careful manner and studied their shear piezoelectric properties. Moreover, the piezoelectric constant was determined using the dielectric resonance method, a technique that has hardly ever reported on polymers.

The objectives of this study are

(i) To investigate the F_c and X_c dependence on the shear piezoelectricity in PLLA

(ii) To study the dielectric and piezoelectric relaxations in the structurally controlled semicrystalline PLLA films

This study aimed to directly compare the influence of thermally stretch polymer-chain orientation on the piezoelectric property of PLLA. This involved using a series of annealing temperatures and uniaxial expansion which is associated with the strain ratio and expansion temperature. Dielectric resonance method was used in analyzing the piezoelectric constant of the PLLA film. We discuss the piezoelectric relaxation observed in the PLLA samples particularly focusing on the highly crystalline and oriented samples and present a structural model for uniaxially oriented PLLA fibers where the crystal transformation is taken into consideration.

1.5 Thesis structure

In the first chapter, a brief history of piezoelectric materials and their applications, as well as the information on piezoelectricity in polymers and an introduction to poly-L-lactic acid and its industrial applications are deliberated. The following section contains a discussion of the problem statement, the objectives of the study, as well as the structure of the thesis.

Chapter 2 presents the fundamental principal of dielectric and piezoelectric in materials. This chapter also includes literature review of PLLA, synthesis methods of PLLA, chain conformation and crystal structure, effect of crystallinity on dielectric and piezoelectric relaxations in polymers.

Chapter 3 discusses the fabrication process of the materials as well as the characterization techniques used in this study. The background research on each instrument is briefly described.

The structural and thermal properties of PLLA measured using WAXS and DSC were discussed in chapter 4. The dielectric spectra were used to describe the molecular dynamics of amorphous and semicrystalline PLLA polymers. Moreover, the piezoelectric resonance of the PLLA polymers were thoroughly analyzed and discussed in this chapter.

Finally, chapter 5 summarizes the findings of the overall study in this thesis and suggests several future research directions on this field.

CHAPTER 2: LITERATURE REVIEW

2.1 Introduction

This chapter examines the fundamental mechanisms that underlie the dielectric and piezoelectric properties of polymers, as well as their applications. Also included are the mathematical equations relating to dielectric and piezoelectric materials. Finally, in the final section, we discuss the origin of piezoelectricity in poly-L-lactic acid (PLLA) polymer.

2.2 Dielectrics

Substances are classified into two broad categories: conductors and insulators (or dielectrics). In contrast to metals, which allow charges to move freely inside the material, dielectrics bind all charges to specific atoms and molecules. These are referred to as bound charges. However, these charges can be moved within an atom or molecule. While these microscopic displacements are not as dramatic as charge rearrangement in a conductor, their cumulative effect accounts for dielectric materials' unique behaviour. When a dielectric material is exposed to an external electric field, it becomes polarized, acquiring a dipole moment. Polarizability is a characteristic of dielectrics. Polarizability occurs as a result of the fact that molecules, contain both positive and negative charges (nuclei) (electrons). When an electric field applied on a molecule, positive charges are displaced in the direction of the field, and negative charges are pushed in the opposite direction. Thus, the action is to separate the opposite charges, polarizing the molecule.

The polarization of a dielectric material, P (C/m^2), is defined as the dipole moment per unit volume and it is a macroscopic quantity. Suppose the medium is isotropic and the induced polarization, P is parallel to E with a coefficient of proportionality that is independent of direction

$$P = \varepsilon_o \chi_e E \tag{2.11}$$

The constant χ_e is the electric susceptibility of the medium and ε_o is the vacuum permittivity. The χ_e is related to dielectric permittivity via:

$$\varepsilon = \varepsilon_o(1 + \chi_e) \tag{2.12}$$

On a microscopic scale, the degree of polarization depends on the polarizability of the molecules (repeat units) and the local electric field, E_{loc},

$$P = \sum_i n_i a_i E_{loc} \tag{2.13}$$

where α_i is the polarizability of a structural element i and n_i is its concentration (number of structural elements i per unit volume),

The relationship between the polarization, P, and the applied electric field E is

$$P = \varepsilon_0 E(\varepsilon_r - 1) \tag{2.14}$$

and the relationship between the local field, E_{loc}, and the polarization, P, is

$$E_{loc} = E + P/(3\varepsilon_0) \tag{2.15}$$

and combining these expressions gives the *Clausius-Mosotti* relation:

$$\frac{\varepsilon_r - 1}{\varepsilon_r + 2} = \frac{\sum_i n_i a_i}{3\varepsilon_0} \tag{2.16}$$

There are three mode of polarizations which are electronic, atomic and orientational polarization as illustrated in Figure 2.1. Electronic polarization is caused by the displacement of the local electronic charge cloud around nucleus due to the applied electric field while atomic polarization is the displacement atomic nuclei relative to one another. Orientation polarization is the alignment of dipoles due to an external electric field.

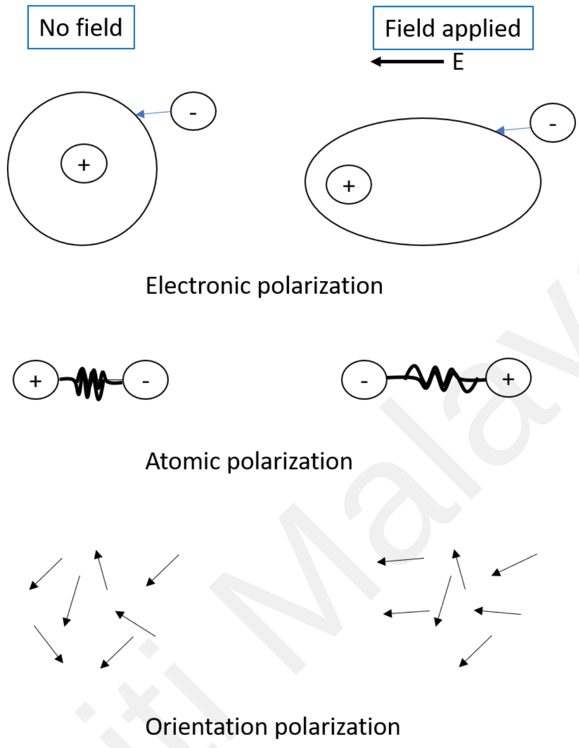

Figure 2.1: Illustration of three types of polarization

Polarization contributes to permittivity only up to a particular frequency range, which is determined by the mass of the charged particles and the type of bond. For example, only electrons with a very low mass can follow an applied oscillating electric field in the visual range, but the atomic polarization of heavier and slower-moving nuclei tapers off above infrared frequencies. Permanent dipole moment orientation polarization is notably "sluggish" and takes significantly longer than electronic and atomic polarization. As a result, it happens only below the microwave region.

Dielectric relaxation is the time required for a medium to reach equilibrium polarization following an abrupt change in the electric field. This delay is caused by the 'friction' between the charge displacements and the permanent reorientation of the dipole moment (Alegria & Colmenero, 2016).

The complex permittivity, $\varepsilon^* = \varepsilon' - i\varepsilon''$ (where ε' is the real permittivity and ε'' is the imaginary permittivity), computed by applying alternating electric field E, with an amplitude E_0, and angular frequency ω, across a dielectric material:

$$E = E_0 cos\omega t \tag{2.17}$$

The electric field produce polarization, which alternates in direction. If the frequency is high enough, the orientation of the dipoles, will inevitably lag behind the applied electric field. The phase lag is denoted as δ and this phase lag in the electric displacement D will be

$$D = D_0 \cos(\omega t - \delta) \tag{2.18}$$

which can be written as:

$$D = D_1 cos\omega t + D_2 sin\omega t \tag{2.19}$$

where

$$D_1 = D_0 cos\delta \qquad \text{and} \qquad D_2 = D_0 sin\delta \tag{2.20}$$

From the above equations, the complex dielectric permittivity is defined as

$$\varepsilon_r' = \frac{D_1}{\varepsilon_0 E_0} \qquad \text{and} \qquad \varepsilon_r'' = \frac{D_2}{\varepsilon_0 E_0} \tag{2.21}$$

linked by the relation

$$\frac{\varepsilon_r''}{\varepsilon_r'} = tan\delta \tag{2.22}$$

Typically, dielectric relaxation processes are investigated using a combination of models. The Debye function is a fundamental theoretical function that is used to characterize the experimentally observed dielectric spectra in both the frequency and time domains. The Debye function for the frequency dependence of complex permittivity, ε^* is written as:

$$\varepsilon^* = \varepsilon_\infty + \frac{\Delta\varepsilon_r}{1+i\omega\tau_D} \tag{2.23}$$

where $\Delta\varepsilon_r = \varepsilon_S - \varepsilon_\infty$ is the dielectric relaxation strength. The ε_S is the static dielectric permittivity, ε_∞ is the infinite relative dielectric permittivity and τ_D is the Debye relaxation time where the maximal loss occurs. In most cases, the relaxation peaks are asymmetric with high frequency tail where its half width of measured loss peaks is much broader as predicted by the Debye function and it is called as a non-Debye (non –ideal) relaxation behavior. As a result, the broadening of the dielectric function can be described by the Cole-Cole function (Schönhals & Kremer, 2003):

$$\varepsilon^* = \varepsilon_\infty + \frac{\Delta\varepsilon_r}{1+(i\omega\tau_{cc})^\alpha} \tag{2.24}$$

where α describes the symmetrical broadening of the relaxation peaks. In the Debye function, $\alpha = 1$ while in the Cole-Cole function α is $0 < \alpha \leq 1$. The Cole-Cole relaxation time, τ_{cc} denotes the position of a maximal loss by $\omega = 1/\tau_{cc}$.

In addition, the complex dielectric function can have an asymmetric broadening peak described by the Cole-Davidson function (Schönhals & Kremer, 2003):

$$\varepsilon^* = \varepsilon_\infty + \frac{\Delta\varepsilon_r}{(1+i\omega\tau_{CD})^\beta} \tag{2.25}$$

The parameter $\beta(0 < \beta \leq 1)$ describes the asymmetric broadening of the relaxation function. When β =1, the Debye-function is recovered again. It should be noted that the characteristic relaxation time of this asymmetric model function like the Cole- Davidson function does not coincide with the relaxation time which is related to the position of maximal loss. The relationship of both quantities depends on the shape parameter.

A more general function was then introduced by Havriliak and Negami (HN-function) by including both combination of the Cole-Cole and the Cole-Davidson function (Schönhals & Kremer, 2003):

$$\varepsilon^* = \varepsilon_\infty + \frac{\Delta\varepsilon_r}{(1+(i\omega\tau_{CD})^\alpha)^\beta} \tag{2.26}$$

The symmetric and asymmetric broadening of the complex dielectric function can be described by the fractional shape parameters, α and β in which $0 < \alpha,\ \alpha\beta \leq 1$. The parameters α and β are related to the limiting behavior of the complex dielectric function at low and high frequencies. By analyzing the frequency and temperature dependence of the complex permittivity; the dielectric strength, phase transition, transition temperature and frequency relaxation involved in the system can be identified. The HN-function will be applied to fit the complex permittivity for a complete description of the isolated regions that involved in the system.

2.3 Piezoelectricity

Piezoelectricity is the cross coupling effect between elastic variables such as stress and strain and dielectric variables such as electric displacement and electric field (T. Furukawa, 1989). The relation between these variables is shown in Figure 2.2.

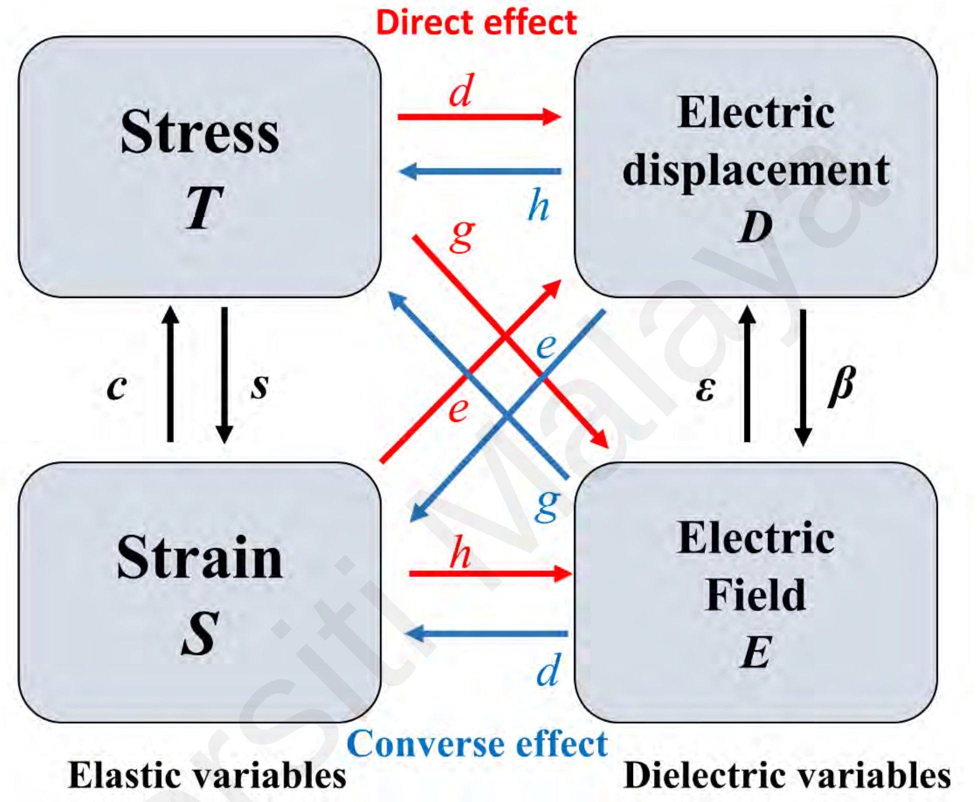

Figure 2.2: Linear electromechanical equations

The coefficients of piezoelectricity are determined by the relationship between elastic and dielectric variables. The red arrow pointing from elastic variables to dielectric variables represents the direct piezoelectric effect, whereas the blue arrow pointing from dielectric variables to elastic variables represents the reverse piezoelectric effect (see Figure 2.2). As shown in Figure 2.3, the direct piezoelectric effect occurs when externally applied mechanical stress induces electrical polarization in particular materials (a). In contrast, the externally applied electric field causes mechanical strain in inverse piezoelectric effect (b) (Fukada, 1995).

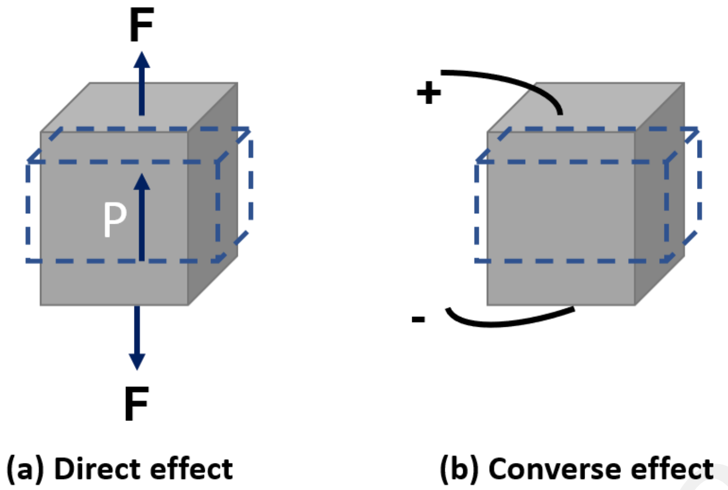

Figure 2.3: Macroscopic piezoelectric effect

The electromechanical equation of piezoelectric materials can be described using a combination of following variables (Takeo Furukawa & Fukada, 1976):

$$D_i = \varepsilon_{ik}^{T} E_k + 4\pi d_{il} T_l$$

$$S_j = d_{jk} E_k + s_{jl}^{E} T_l$$

$$D_i = \varepsilon_{ik}^{S} E_k + 4\pi e_{il} S_l$$

$$T_j = -e_{jk} E_k + c_{jl}^{E} S_l$$

$$E_i = \beta_{ik}^{T} D_k - g_{il} T_l$$

$$S_j = \frac{1}{4\pi} g_{jk} D_k + s_{jl}^{D} T_l$$

$$E_i = \beta_{ik}^{S} D_k - h_{il} S_l$$

$$T_j = -\frac{1}{4\pi} h_{jk} D_k + c_{jl}^D S_l \tag{2.27}$$

where *i, k* = 1, 2, 3 and *j, l* =1, 2, …6 with repetition of a suffix implies summation corresponding to that suffix. Superscripts *S* and *T* denotes that all strains and stresses in the material are constant while superscripts *D* and *E* denotes that the compliance measured with open circuit and closed circuit respectively. The displacement, D_i and electric field, E_i are the dielectric variables while stress, T_j and strain, S_j are the elastic variables, respectively. The symbol $\varepsilon_{ik}$is the dielectric constant, β_{ik} is the inverse dielectric constant, the s_{jl} is the elastic compliance and c_{jl} is the elastic constant.

The piezoelectric constants are defined as follows, which is the first definition, refers to direct effect and the second one to the converse effect (Takeo Furukawa & Fukada, 1976; Mellinger, 2003):

$$d_{ij} = (\frac{\partial D_i}{\partial T_j})_E = (\frac{\partial S_j}{\partial E_i})_T$$

$$e_{ij} = (\frac{\partial D_i}{\partial S_j})_E = -(\frac{\partial T_j}{\partial E_i})_S$$

$$g_{ij} = -(\frac{\partial E_i}{\partial T_j})_D = (\frac{\partial S_j}{\partial D_i})_T$$

$$h_{ij} = -(\frac{\partial E_i}{\partial S_j})_D = -(\frac{\partial T_j}{\partial D_i})_S \tag{2.28}$$

The four piezoelectric coefficients are interrelated through the following equations:

$$\frac{d_{ij}}{e_{il}} = s_{jl}^E; \qquad \frac{g_{ij}}{h_{il}} = s_{jl}^D$$

$$\frac{d_{ij}}{g_{kj}} = \frac{\varepsilon_{ik}^T}{4\pi}; \qquad \frac{e_{ij}}{h_{kj}} = \frac{\varepsilon_{ik}^S}{4\pi} \tag{2.29}$$

The electromechanical coupling factor is related to the s and ε via

$$\frac{s^E}{s^D} = \frac{\varepsilon^S}{\varepsilon^T} = 1 - k^2 \tag{2.30}$$

where the designation of a boundary condition in s and ε is omitted because of the relatively small value of k.

Piezoelectric can be distinguished into four different cases according to the direction of electric displacement and component of mechanical stress as schematically displayed in Figure 2.4 (Tichý et al., 2010). The piezoelectric polarization parallel to the normal mechanical stress is known as the longitudinal piezoelectric effect (see symbol L in Figure 2.4). On the other hand, the piezoelectric polarization perpendicular to the applied normal stress is called as transversal effect (see symbol T in Figure 2.4). Application of shear stress cause result in the piezoelectric polarization perpendicular to the plane of the applied shear and called as the longitudinal shear piezoelectric effect (see symbol S_L in Figure 2.4). The piezoelectric polarization parallel to the plane of the applied shear stress is the transversal shear piezoelectric (see symbol S_T in Figure 2.4). The longitudinal shear piezoelectric effect will be explained in detail because it is the only piezoelectric effect observed for our material.

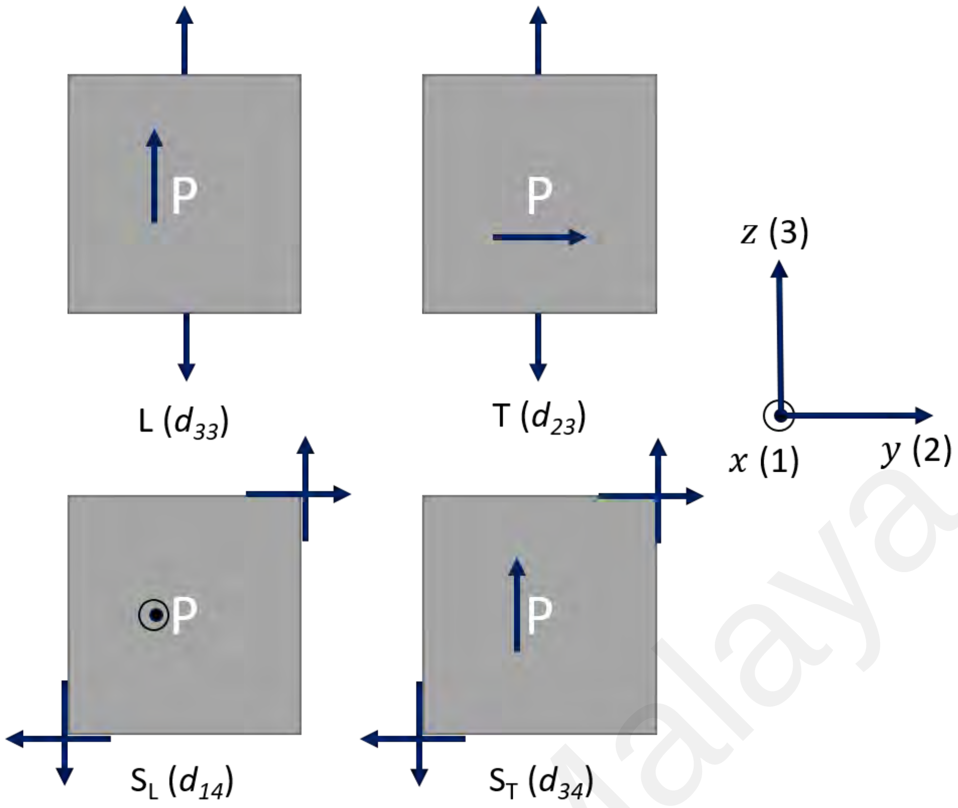

Figure 2.4: Mechanical and piezoelectric stress examples in the four possible orientations.

2.4 Piezoelectric polymers

Piezoelectric polymers are classified into two types: Class 1 and Class 2. Class 1 is a poled polar polymer, which generates piezoelectricity when subjected to a high dc electric field (poling). Class 2 piezoelectric polymers are optically active polymers in which mechanical drawing causes the chain molecules to be oriented in a P_2 (second order Legendre polynomial) orientation, resulting in piezoelectricity if the polymer is chiral. Polyvinylidene fluoride (PVDF) is an example of a Class 1 piezoelectric polymer, whereas poly-L-lactic acid (PLLA) is an example of a Class 2 piezoelectric polymer. Table 2.1 illustrates an example of a Class 2 polymer. Among the polymers, PLLA exhibits the highest shear piezoelectricity. Table 2.1 shows the example of Class 2 polymers and its corresponding shear piezoelectric constant, d_{14}. PLLA is the polymer with the highest shear piezoelectricity when compared to the other.

Table 2.1: Comparison of the piezoelectric constant of three optically active polymers.

Polymers	Piezoelectric constant, d_{14} (pC/N)	Reference
Polypropelene oxide	0.1	(Fukada, 2000)
Poly-β-hydroxybutarate	1.3	(Fukada & Ando, 1986)
Poly-lactic acid	10.0	(Fukada, 2000)
Polysuccinimides	1.8	(Tanimoto et al., 2015)
Cellulose	0.4	(Fukada, 1968)

2.5 Poly-l-lactic acid (PLLA)

2.5.1 Synthesis of PLLA

Poly(lactic) acid (PLA) is an aliphatic polyester that is usually produced from *α*-hydroxy acids, such as polyglycolic acid or polymandelic acid. Swedish chemist Scheele has first produced the lactic acid as a basic building block for PLA in 1970 and mostly used in the United States for food-related applications. Lactic acid (2-hydroxy propionic acid) is made by bacterial fermentation of carbohydrates which produced D(-)- and L(+)-isomers as shown in Figure 2.5.

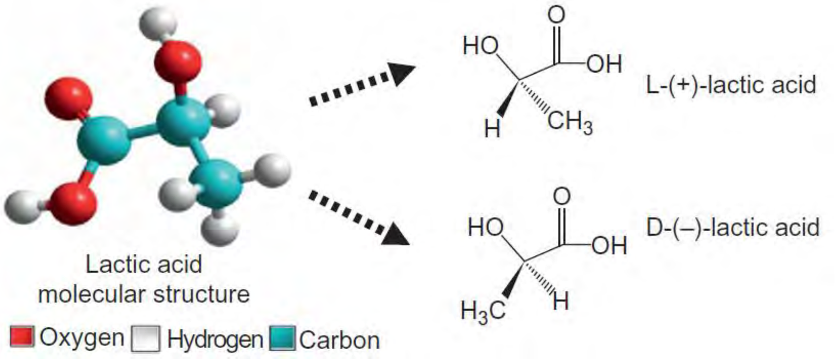

Figure 2.5: Stereoisomers of lactic acid (Copyright permission from Elsevier (Lowe, 1952a))

PLA can be converted to high-molecular-weight (M_W > 100,000) amorphous or crystalline polymers by collecting, purifying, and ring-open polymerizing (ROP) lactide. Carothers et al. (1932) demonstrated the first ROP of lactide, but they did not achieve high molecular weight until 1954, when and Lowe, (1952) enhanced lactide purifying processes by adding catalyst. Figure 2.6 showed polymerization reaction of PLA in synthesizing high molecular weight PLA.

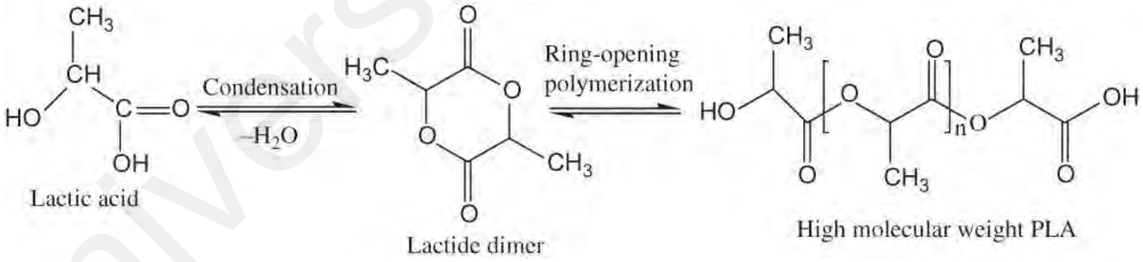

Figure 2.6: Polymerization reaction of lactic acid (Ahmed & Varshney, 2011).

Polymerization of L-lactide produce poly-L-lactic acid (PLLA) while polymerization of D-lactide produce poly-D-lactic acid (PDLA) crystalline polymers. The combination of L-lactide and D-lactide produce poly(DL-lactide) which is an amorphous polymer with a melting temperature between 145-175°C. The properties of polylactide depend on the ratio and distribution of the two isomers and the molecular weight.

2.5.2 Chain conformations and crystal structures

PLLA crystallizes into at least three polymorphs (α-, β-, and γ-) depending on the preparation condition. The α-form was first proposed as a pseudo-orthorhombic structure (a = 10.6 Å, b = 6.1 Å and c = 28.8 Å) containing two antiparallel chains in a unit cell by de Oca & Ward (2007), De Santis & Kovacs (1968) and Kobayashi et al. (1995). The α-form is found at relatively low drawing temperatures while the β-form is prepared at a high drawing ratios and temperatures. For the former, an orthorhombic unit cell is proposed (a = 10.31 Å, b = 18.21 Å and c = 9.00 Å) containing six chains. The chain conformation of β-form PLLA is 3/1 helices. However, the transformation from α- to β form is difficult to achieve. The α-form PLLA is the most stable and exhibits a well-defined fiber diffraction pattern with s(3*10/7) chain conformation (Hoogsteen et al., 1990; Kobayashi et al., 1995; Sasaki & Asakura, 2003). In the α-form PLLA, the C=O dipoles are randomly oriented along the main chain. To produce piezoelectricity, the α-crystalline chains must be thermally stretched from randomly oriented molecular chains to molecular chains aligned along the extended direction (Sultana et al., 2017; Tajitsu, 2007). Another PLLA polymorph is the γ-form, which is an orthorhombic unit cell with two 3_1-helical helices aligned antiparallel. It can be produced epitaxially on a substrate such as hexamethylbenzene (Laurent Cartier et al., 2000)

2.5.3 Effect of crystallinity on dielectric relaxations

Recent research indicates that crystallinity has an effect on relaxation dynamics reported the evolution of relaxation dynamics during PLLA isothermal crystallization using in-situ dielectric spectroscopy (Ana Rita Brás et al., 2006; Hikosaka et al., 2011; Kanchanasopa & Runt, 2004; Kortaberria et al., 2007).

During crystallization of fully amorphous sample, two main α relaxation could be observed. The α_{NA} occurred in mobile amorphous phase (MAP) observed at high frequency and disappear when the crystallization is complete while α_{SC} occurred in rigid amorphous phase (RAP), observed at low frequency as shown in Figure 2.7(a) (Dionísio et al., 2005). The RAP is the amorphous phase confined between lamellae that occurred during crystallization and can be proved by the existence of Hedrite, the intermediate structure between single lamellar crystal and mature spherulite in the Atomic Force Microscopy (AFM) (refer to Figure 2.7(b)) (Bassett & Vaughan, 1985; Kortaberria et al., 2007). β relaxation is localized motion that rise from the rotation of the side group and it can be observed below glass transition temperature, T_g at higher frequencies. Additionally, there is a relaxation associated with normal mode, but it is extremely difficult to detect due to the strong conductivity at low frequencies.

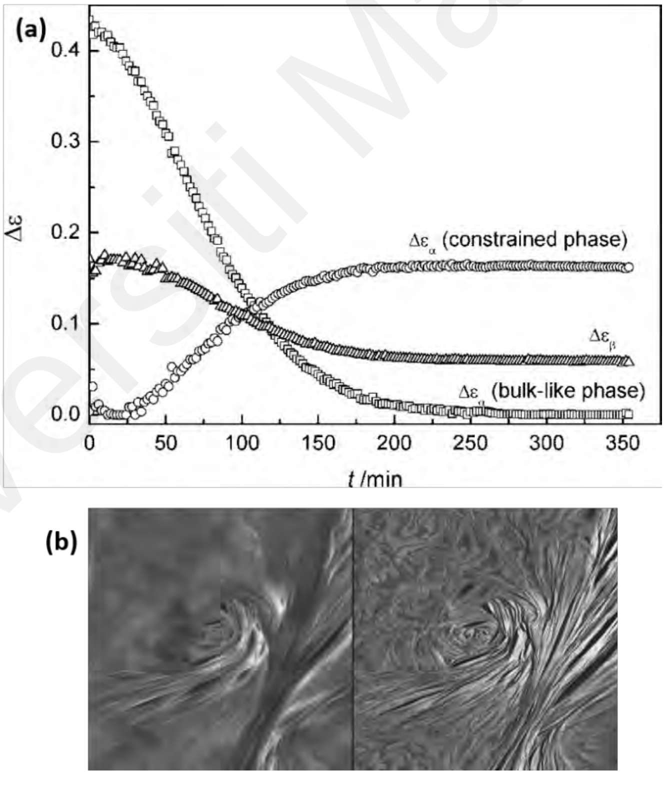

Figure 2.7: (a) Evolution of dielectric strength of three relaxations in PLLA during the crystallization and (b) the AFM image during crystallization at 150°C after 35 minutes (Copyright permission from John Wiley & Son (Dionísio et al., 2005)).

To investigate α_{SC}, PLLA samples with varying percentages of crystallinity, X_c, were measured using dielectric spectroscopy (A. R. Brás et al., 2008). The results showed that the α_{SC} shifted to higher frequencies/ lower temperature and the dielectric strength, $\Delta\varepsilon$ decreases as the crystallinity increase (see Figure 2.8). This is because the thickness of the RAP increase which is shown from the WAXS and SAXS studies (Wang et al., 2006). Additionally, the RAP could also change with temperature variation. It can be observed that as the temperature increase, the dielectric strength increase. This study indicates that the stiff amorphous phase is not rigid at all, but rather relaxes between the MAP glass transition and the crystalline phase's melting point.

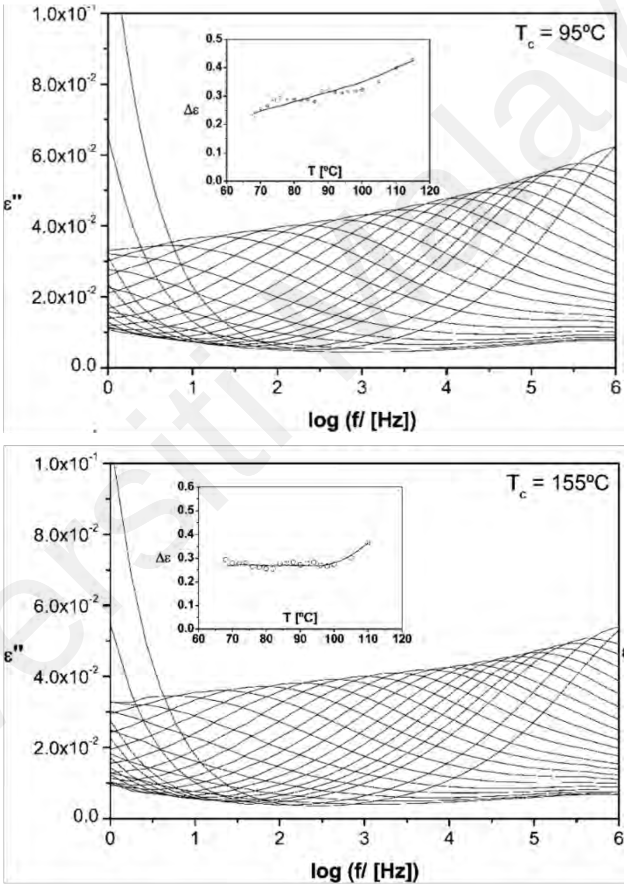

Figure 2.8: Isothermal dielectric loss spectra of semicrystalline PLLA for α relaxation from 60°C to 100°C with different crystallization temperature, T_c. Inset presents the temperature dependence of dielectric strength, $\Delta\varepsilon$ (Reprinted with permission from American Chemical Society (A. R. Brás et al., 2008)).

The effect of crystallinity on the molecular relaxation time, for the amorphous and semicrystalline sample was investigated (Ana Rita Brás et al., 2006; Mijović & Sy, 2002). There is no statistically significant difference between both relaxations when the crystallinity is varied, as the data falls on the same curve. The glass-forming α process is well-known for diverging from the thermally activated Arrhenius functional form and exhibiting significantly increased temperature dependence. Such behavior is modelled using the Vogel-Fulcher-Tammann (VFT).

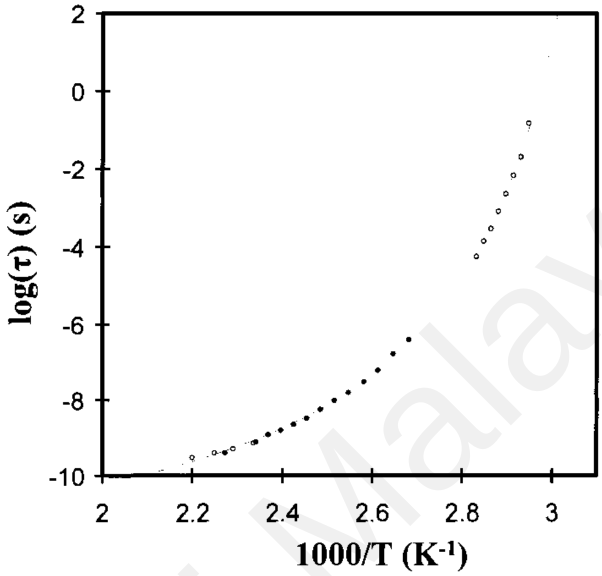

Figure 2.9: Average relaxation time as a function of reciprocal temperature for wholly amorphous (open circle) and crystalline (solid circle) PLLA (Copyright permission from John Wiley & Sons (Ana Rita Brás et al., 2006)).

2.5.4 Piezoelectricity of PLLA and resonance measurements

The piezoelectric phenomenon in chiral polymers such as PLLA originates in the crystalline regions, which have a defined molecular arrangement, and each crystalline region demonstrates microscopic piezoelectricity. Cartesian coordinate systems assigned to the oriented PLLA film is shown in Figure 2.10. A rectangular coordinate was assigned to the film, in which the z-axis (3-direction) was taken in the direction of orientation, y-axis (2-direction) normal to the film. The polarization in the y-axis is related to the shear stress in the film. If an electric field is applied in the x-axis (1-direction) of the film, shear strain is induced perpendicular to the field direction. The shear strain, d_{36}, vanishes for films with a uniaxial orientation. The piezoelectric constants of PLLA are specified by d_{14} and d_{25} where the $d_{25} = -d_{14}$ by symmetry (see Figure 2.10).

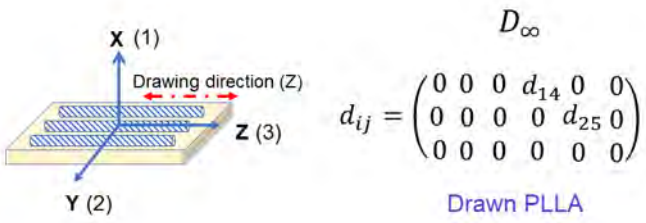

Figure 2.10: Schematic diagram of macro symmetry in PLLA due to mechanical drawing.

The investigation of piezoelectric resonances in the dielectric spectrum is a very versatile approach. In comparison to static or dynamic mechanical measurements or optical interferometry, dielectric spectroscopy has the advantage of determining several critical material parameters in a single measurement using readily available laboratory equipment, provided the sample can be accessed under stress-free or limited mechanical boundary conditions. In a typical experiment, the experimental data are fitted to the theoretical expression for the complex permittivity $\varepsilon^*(\omega)$ of frequency dependence. The material parameters in the weak signal limit can therefore be simply determined from the fitted parameters. The electromechanical coupling coefficients, *k,* elastic constant, *c,* dielectric permittivity, ε and the piezoelectric matrix components, d_{14} and e_{14} are obtained from the dielectric resonance spectrum.

For a rectangular piezoelectric polymer film, three modes of piezoelectric resonant peaks are observed, i.e., length extension (LE), width extension (WE) and thickness extension (TE) modes as shown in Figure 2.11.

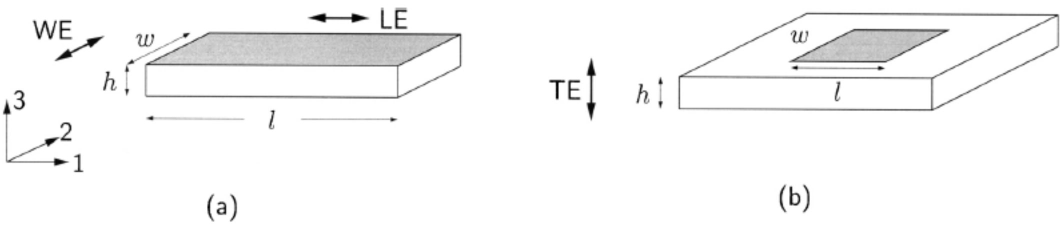

Figure 2.11: (a) Length extension (LE) and width extension (WE) mode (b) thickness extension (TE) mode.

Example of the three-extension modes that are observed in the dielectric spectrum of polyvinylidene fluoride PVDF) is shown in Figure 2.12.

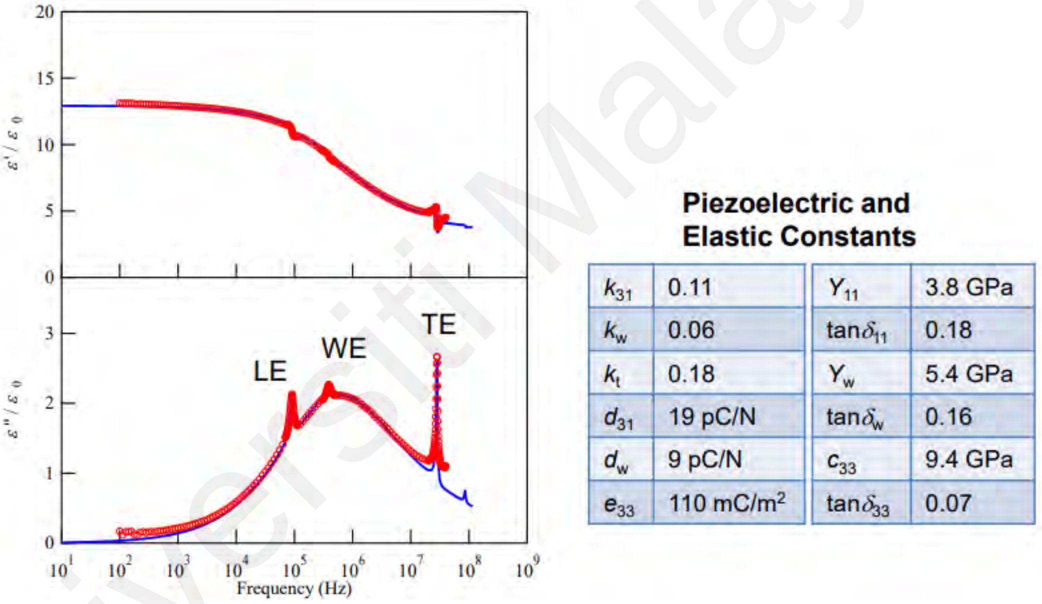

Piezoelectric and Elastic Constants

k_{31}	0.11	Y_{11}	3.8 GPa
k_w	0.06	$\tan\delta_{11}$	0.18
k_t	0.18	Y_w	5.4 GPa
d_{31}	19 pC/N	$\tan\delta_w$	0.16
d_w	9 pC/N	c_{33}	9.4 GPa
e_{33}	110 mC/m²	$\tan\delta_{33}$	0.07

Figure 2.12: The observed (red circle) and fitted (blue line) curve of dielectric permittivity (sample dimension: 20 mm x 7 mm x 40 μm).

The extension modes that are observed can be fitted using the equation shown below:

The complex permittivity $\varepsilon^*(\omega) = \varepsilon'(\omega) - i\varepsilon''(\omega)$ for length extension LE, width extension WE and thickness extension TE modes is given by (Nishi, 1999);

$$\varepsilon^* = \varepsilon^S \frac{\left(1+\frac{k_l^2}{1-k_l^2}\frac{\tan a_l f}{a_l f}\right)\left(1+\frac{k_w^2}{1-k_w^2}\frac{\tan a_w f}{a_w f}\right)}{1-k_t^2\frac{\tan a_t f}{a_t f}} \tag{2.31}$$

where ε^{s} is the dielectric relaxation and in this case we refer ε^{s} to HN function (see Eq. 2.26).

For LE mode, a_l and k_l are computed as

$$a_l = \frac{\pi}{2f_l} = \pi t\sqrt{\rho s_{11}^{E*}} \quad \text{and} \quad k_l^2 = \frac{d_{31}^2}{\varepsilon_{33}^T s_{11}^E} \tag{2.32}$$

and ρ is the density of the material, *l* is the length of the film, s_{11}^E is the compliance at constant electric field, s_{11}^{E*} is the imaginary compliance, $f_l$is the complex anti-resonance frequency of LE mode, *k*$_l$ is the electromechanical coupling factor along the length direction, *d* is the piezoelectric constant, ε^{T} is the dielectric permittivity of the sample at constant stress.

In the WE mode, the a_w and k_w are defined as;

$$a_w = \frac{\pi}{2f_w} = \pi w\sqrt{\rho(s_{22}^{E*} - s_{12}^{E*2}/s_{11}^{E*})}$$

$$k_w^2 = \frac{(d_{32} - \frac{d_{31}s_{12}^E}{s_{11}^E})^2}{\varepsilon_{33}^T(1-k_l^2)(s_{22}^E - \frac{s_{12}^{E2}}{s_{11}^E})} \tag{2.33}$$

where f_w is the anti-resonance frequency of WE mode, *w* is the width of the film, k_w is the electromechanical coupling factor along the width direction and d_{32} is the piezoelectric constant.

The resonance occurs at higher frequency (>10MHz) is described using TE mode where:

$$a_t = \frac{\pi}{2f_t} = \pi t\sqrt{\rho/c_{33}^{D*}} \quad \text{and} \quad k_t^2 = \frac{e_{33}^2}{\varepsilon_{33}^S c_{33}^D} \tag{2.34}$$

where f_t is the anti-resonance frequency at TE mode, t is film thickness, k_t is the electromechanical coupling factor in thickness direction, c_{33}^D is the elastic constant at a constant electric displacement.

2.5.5 Basic Analysis of drawn chiral polymers' piezoelectric resonance

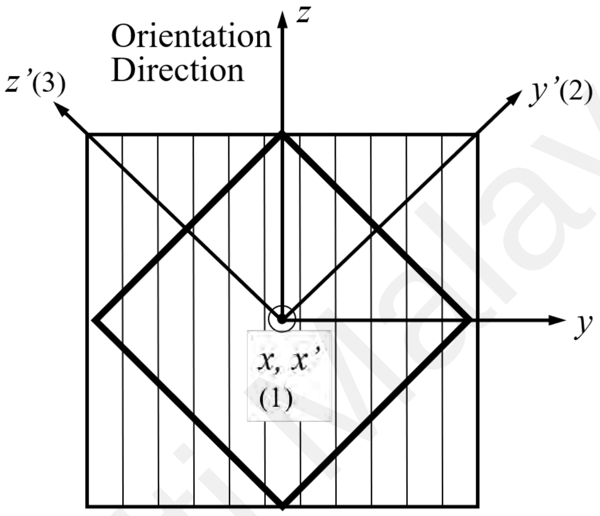

Figure 2.13: Cartesian coordinate systems assigned to uniaxially oriented films (*x,y,z*) and 45° cut for square sample (x',y',z').

The piezoelectric constants of the uniaxially oriented chiral polymer are d_{14} and e_{14}. The component *ij*=14 expresses the dielectric displacement, D_1 in the *x*-direction induced by the shear stress T_4 in *yz* plane or shear strain, S_4 in the *yz* plane induced by the electric field, E_1 in the *x*–direction, respectively. The *x*-axis is assigned to the thickness direction of the film, the *z*-axis is along the orientation direction, and *y*-axis is orthogonal to them (Figure 2.13). For the piezoelectric resonant measurement, a 45-degree cut sample is used, so that the shear stress and strain are converted to normal stress and strain. In Figure 2.13, we assigned (*x', y', z'*) which is 45° rotated with respect to the original (*x, y, z*) axes, and the respected coordinate transformation is expressed as below.

$$\begin{bmatrix} x' \\ y' \\ z' \end{bmatrix} = \begin{bmatrix} 1 & O & 0 \\ 0 & \cos\theta & \sin\theta \\ 0 & -\sin\theta & \cos\theta \end{bmatrix} \begin{bmatrix} x \\ y \\ z \end{bmatrix}, \theta=45° \quad \begin{bmatrix} x' \\ y' \\ z' \end{bmatrix} = \begin{bmatrix} 1 & 0 & 0 \\ 0 & 1/\sqrt{2} & 1/\sqrt{2} \\ 0 & -1/\sqrt{2} & 1/\sqrt{2} \end{bmatrix} \begin{bmatrix} x \\ y \\ z \end{bmatrix} \tag{2.35}$$

The transformation matrix (b_{ij}) of strain is calculated as follows;

$$[b_{ij}] = \begin{bmatrix} {a_{11}}^2 & {a_{12}}^2 & {a_{13}}^2 & a_{12}a_{13} & a_{13}a_{11} & a_{11}a_{12} \\ {a_{21}}^2 & {a_{22}}^2 & {a_{22}}^2 & a_{22}a_{23} & a_{23}a_{21} & a_{21}a_{22} \\ {a_{31}}^2 & {a_{32}}^2 & {a_{22}}^2 & a_{32}a_{33} & a_{32}a_{31} & a_{31}a_{32} \\ 2a_{21}a_{31} & 2a_{22}a_{32} & 2a_{23}a_{33} & a_{22}a_{33}+a_{23}a_{32} & a_{22}a_{33}+a_{23}a_{32} & a_{22}a_{33}+a_{23}a_{32} \\ 2a_{31}a_{11} & 2a_{32}a_{12} & 2a_{33}a_{13} & a_{32}a_{13}+a_{33}a_{12} & a_{33}a_{11}+a_{31}a_{13} & a_{31}a_{12}+a_{32}a_{11} \\ 2a_{11}a_{21} & 2a_{12}a_{22} & 2a_{13}a_{23} & a_{12}a_{23}+a_{13}a_{22} & a_{13}a_{21}+a_{11}a_{23} & a_{11}a_{22}+a_{12}a_{21} \end{bmatrix} \tag{2.36}$$

$$\begin{bmatrix} {S_1}' \\ {S_2}' \\ {S_3}' \\ {S_4}' \\ {S_5}' \\ {S_6}' \end{bmatrix} = \begin{bmatrix} 1 & 0 & 0 & 0 & 0 & 0 \\ 0 & cos^2\,\theta & sin^2\,\theta & sin\,\theta\,cos\,\theta & 0 & 0 \\ 0 & sin^2\,\theta & cos^2\,\theta & -sin\,\theta\,cos\,\theta & 0 & 0 \\ 0 & -2\,sin\,\theta\,cos\,\theta & 2\,sin\,\theta\,cos\,\theta & cos^2\,\theta - sin^2\,\theta & 0 & 0 \\ 0 & 0 & 0 & 0 & cos\,\theta & -sin\,\theta \\ 0 & 0 & 0 & 0 & sin\,\theta & cos\,\theta \end{bmatrix} \begin{bmatrix} S_1 \\ S_2 \\ S_3 \\ S_4 \\ S_5 \\ S_6 \end{bmatrix} \tag{2.37}$$

$$\text{when } \theta = \frac{\pi}{4}, \quad \begin{bmatrix} {S_1}' \\ {S_2}' \\ {S_3}' \\ {S_4}' \\ {S_5}' \\ {S_6}' \end{bmatrix} = \begin{bmatrix} 1 & 0 & 0 & 0 & 0 & 0 \\ 0 & 1/2 & 1/2 & 1/2 & 0 & 0 \\ 0 & 1/2 & 1/2 & -1/2 & 0 & 0 \\ 0 & -1 & 1 & 0 & 0 & 0 \\ 0 & 0 & 0 & 0 & 1/\sqrt{2} & -1/\sqrt{2} \\ 0 & 0 & 0 & 0 & 1/\sqrt{2} & 1/\sqrt{2} \end{bmatrix} \begin{bmatrix} S_1 \\ S_2 \\ S_3 \\ S_4 \\ S_5 \\ S_6 \end{bmatrix} \tag{2.38}$$

Therefore, the shear strain, S_4 is expressed as,

$$s_2' = \frac{S_4}{2} \quad \text{and} \quad s_3' = \frac{-S_4}{2} \tag{2.39}$$

The transformation matrix of stress, T is obtained by transposing the θ in Eq. (2.35) and calculated as follows;

$$\begin{bmatrix} T_1 \\ T_2 \\ T_3 \\ T_4 \\ T_5 \\ T_6 \end{bmatrix} = \begin{bmatrix} 1 & 0 & 0 & 0 & 0 & 0 \\ 0 & cos^2\theta & sin^2\theta & -2\,sin\,\theta\,cos\,\theta & 0 & 0 \\ 0 & sin^2\theta & cos^2\theta & 2\,sin\,\theta\,cos\,\theta & 0 & 0 \\ 0 & sin\,\theta\,cos\,\theta & -\,sin\,\theta\,cos\,\theta & cos^2\theta - sin^2\theta & 0 & 0 \\ 0 & 0 & 0 & 0 & cos\,\theta & sin\,\theta \\ 0 & 0 & 0 & 0 & -\,sin\,\theta & cos\,\theta \end{bmatrix} \begin{bmatrix} T_1' \\ T_2' \\ T_3' \\ T_4' \\ T_5' \\ T_6' \end{bmatrix}$$

(2.40)

$$\text{when } \theta = \frac{\pi}{4}, \quad \begin{bmatrix} T_1 \\ T_2 \\ T_3 \\ T_4 \\ T_5 \\ T_6 \end{bmatrix} = \begin{bmatrix} 1 & 0 & 0 & 0 & 0 & 0 \\ 0 & 1/2 & 1/2 & -1 & 0 & 0 \\ 0 & 1/2 & 1/2 & 1 & 0 & 0 \\ 0 & 1/2 & -1/2 & 0 & 0 & 0 \\ 0 & 0 & 0 & 0 & 1/\sqrt{2} & 1/\sqrt{2} \\ 0 & 0 & 0 & 0 & -1/\sqrt{2} & 1/\sqrt{2} \end{bmatrix} \begin{bmatrix} T_1' \\ T_2' \\ T_3' \\ T_4' \\ T_5' \\ T_6' \end{bmatrix} \tag{2.41}$$

For shear stress, T_4 is expressed as;

$$T_4 = \frac{T_2'}{2} - \frac{T_3'}{2} \tag{2.42}$$

The electromechanical equation for a 45° cut sample related to face shear piezoelectricity was computed using the new coordinate system. To simplify the equations, we omit the superscript (′), and thus, S_2' & S_3' are taken to be as S_2 & S_3, respectively. $S_1 = 0$ due to the absence of strain in the thickness direction.

$$D_1 = \varepsilon_{11}^S E_1 + e_{12} S_2 + e_{13} S_3 \tag{2.43}$$

$$T_2 = -e_{12} E_1 + c_{22} S_2 + c_{23} S_3 \tag{2.44}$$

$$T_3 = -e_{13} E_1 + c_{23} S_2 + c_{33} S_3 \tag{2.45}$$

where D_1 is the dielectric displacement, ε_{11}^S is the dielectric constant (clamped condition), E_1 is the electric field in thickness direction, S_3 is the strain, T_2 is the stress, e_{12} is the piezoelectric constant and c_{22} is the elastic constant, respectively. Due to the uniaxial symmetry of the system, $e_{12} = -e_{13}$ and $c_{22} = c_{33}$.

The stress and strain in the square cut sample can be expressed as follows;

$$T_3 = -T_2 \ , \ S_3 = -S_2 \qquad (2.46)$$

As a result, Eqs. (2.43) and (2.44) become

$$D_1 = \varepsilon_{11}^S E_1 + 2e_{12}S_2 \qquad (2.47)$$

$$T_2 = -e_{12}E_1 + (c_{22} - c_{23})S_2 \qquad (2.48)$$

Due to the boundary condition, the stress at resonance frequency is $T_2(\pm l/2) = 0$, thus

$$S_2 = \frac{e_{12}}{c_{22}-c_{23}}E_1 \qquad (2.49)$$

We generate the elastic vibration and strain wave propagation by assuming that the elastic wave propagates along the *y*' direction in the *yz* plane, where the displacement, u_i, and strain, S_i are as follows:

$$u_i = A_i \, sin \frac{\omega x_i}{v_i} \qquad (2.50)$$

$$S_i = \frac{\partial u_i}{\partial x_i} = A_i \frac{\omega}{v_i} cos \frac{\omega x_i}{v_i} \qquad (2.51)$$

A_i is the amplitude and ω is the angular velocity

$$S_2(\pm \frac{l}{2}) = A_2 \frac{\omega}{v_2} cos \frac{\omega l}{2v_2} = e_{12}E_1 \qquad (2.52)$$

$$A_2 = \frac{e_{12}}{\frac{\omega}{v_2} cos \frac{\omega l}{2v_2}} E_1 \qquad (2.53)$$

Insert Eq. (2.53) into (2.52)

$$S_2(x_2) = \frac{cos \frac{\omega x_2}{v_2}}{cos \frac{\omega l}{2v_2}} e_{12}E_1 \qquad (2.54)$$

To get the average strain, we integrate $cos \frac{\omega x_2}{v_2}$, thus

$$S_2 = \frac{\frac{1}{l}\int_{-l/2}^{l/2} cos\frac{\omega x_2}{v_2}dx_2}{cos\frac{\omega l}{2v_2}} e_{12}E_1 = \frac{\frac{v_2}{\omega l}\left[sin\frac{\omega x_2}{v_2}\right]_{-l/2}^{l/2}}{cos\frac{\omega l}{2v_2}} e_{12}E_1 = \frac{v_2/2l}{\pi f} tan\frac{\pi f}{v_2/2l} e_{12}E_1 \tag{2.55}$$

By inserting S2 into Eq. (2.48) and $f_2 = \frac{v_2}{2l}$, we get

$$D_1 = \varepsilon_{11}^S E_1 + 2e_{12}\frac{v_2/2l}{\pi f} tan\frac{\pi f}{v_2/2l} e_{12}E_1 = \varepsilon_{11}^S \left(1 + \frac{2{e_{12}}^2}{\varepsilon_{11}^S(c_{22}-c_{23})}\frac{tan(\pi f/2f_2)}{\pi f/2f_2}\right) E_1 \tag{2.56}$$

The dielectric constant at free motion, ε_{11}^T is related to the dielectric constant with clamped condition, ε_{11}^S using the relation below:

$$\varepsilon_{11}^T = \varepsilon_{11}^S \left(1 + k_{12}^2 \frac{tan(\pi f/2f_2)}{\pi f/2f_2}\right) \tag{2.57}$$

where

$$v_2 = \sqrt{\frac{c_{22}-c_{23}}{\rho}}$$

(2.58)

and

$$k_{12}^2 = \frac{2{e_{12}}^2}{\varepsilon_{11}^S(c_{22}-c_{23})} \tag{2.59}$$

ρ is density of the polymer.

The relation of elastic constant, *c*, coupling coefficient, *k* and piezoelectric constant, *e* between oriented film and 45° cut square sample are

$$c_{22} - c_{23} = 2c_{44}^c \tag{2.60}$$

$${k_{12}}^2 = \frac{2{e_{12}}^2}{\varepsilon_{11}^S(c_{22}-c_{23})} = \frac{{e_{14}^c}^2}{\varepsilon_{11}^S c_{44}^c} = {k_{14}^c}^2 \tag{2.61}$$

$$e_{12} = -e_{13} = {e_{14}}^c \tag{2.62}$$

denoting the polymer crystallites as superscript c in the equation (2.60) to (2.62).

2.5.6 Effect of crystallinity and orientation on piezoelectricity of PLLA

Although PLLA has a complex higher ordered structure with intermingled crystalline and amorphous regions, it is possible to control the degree of crystallinity of PLLA through a thermal annealing process. Therefore, the piezoelectric constant of a PLLA film can be engineered and improved by increasing crystallinity and molecular orientation. Symmetry considerations have shown only one matrix component d_{14} exist which is proportional to the second term of Legendre polynomial, P_2 is also known as the orientation factor, F_c

$$P_2 = \frac{<3cos^2\theta - 1>}{2} \tag{2.63}$$

When only the crystallites are orientated and the amorphous portions remain isotropic, the piezoelectric constant, d_{14} of a semicrystalline polymer is:

$$d_{14} = \frac{\emptyset P_2(d_{14}^c - d_{25}^c)}{2} \tag{2.64}$$

where $\emptyset$ is the volume fraction of the crystallites and the superscript ***c*** refers to the PLLA crystals.

Takeo Furukawa & Fukada (1976) showed a linear relationship between the shear piezoelectricity (d_{14}) and orientation coefficient (F_c) of poly(γ-benzyl L-glutamate) samples. They proposed the following equation to describe the relationship between these parameters and crystallinity:

$$d_{14} = X_c * F_c \frac{(d_{14}^c - d_{25}^c)}{2} \tag{2.65}$$

The $d_{14}^c$and d_{25}^c are the shear piezoelectric constant of a single crystal and X_c is the percentage of crystallinity.

Lovell et al. (2011) has also used this relation to study the effects of crystallinity and orientation on the shear piezoelectricity of polylactic acid. They studied the relation between the piezoelectric with the crystallinity, X_c, orientation, F_c, and the product of $X_c * F_c$. They established and concluded a stronger link between the piezoelectric constant and the product of $X_c * F_c$ (see Figure 2.14). These conclusions, however, should be viewed with caution, as the association between crystallinity and orientation was established using a limited sample of data focusing on low orientation and low crystallinity.

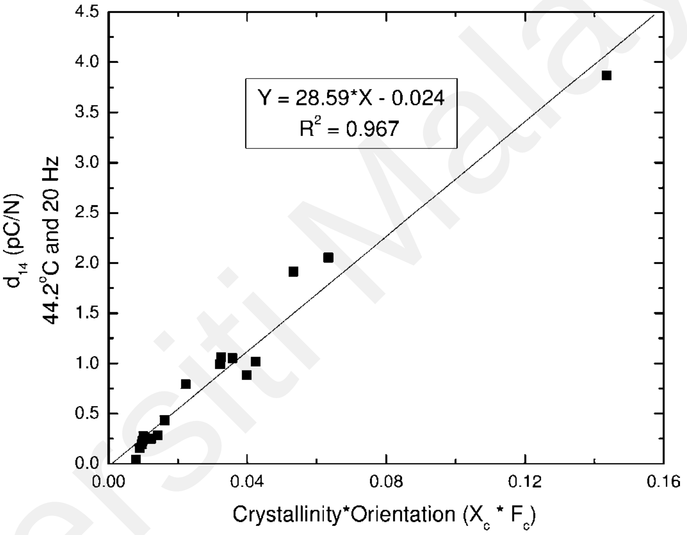

Figure 2.14: Shear piezoelectricity (measured at 44.2 °C and 20 Hz) of polylactic acid versus the product of crystallinity*orientation (X_c*F_c) (Copyright permission from John Wiley & Sons(Lovell et al., 2011)).

CHAPTER 3: METHODOLOGY

3.1 Overview

Sample preparation, structural characterization, and electrical measurement procedures are the three aspects of this chapter. PLLA fabrication procedures, sample drawing ratios, and annealing techniques are covered in the first section. In the second section, the procedures used to characterize the film's structural and thermal properties are discussed. Wide Angle X Ray Scattering (WAXS) is one of the techniques used to measure crystallinity and orientation. Differential Scanning Calorimetry (DSC) was used to study the samples' thermal characteristics. Using DSC, the melting point, glass transition temperature, and crystallization temperature were determined. This chapter ends with a discussion of electrical measurement techniques.

3.2 PLLA film preparation

3.2.1 Uniaxial expansion of the PLLA film

The biaxial PLLA film has a thickness of 50 micrometers and was obtained from Goodfellow Cambridge Limited Enterprise. The PLLA films were cut into a dog bone shape with a width of 3 cm, a length of 2 cm, and a necking width of 2 cm, as illustrated in Figure 3.1. Additionally, a line interval of 0.5 cm was sketched on the film to measure/identify the film's elongation upon drawing.

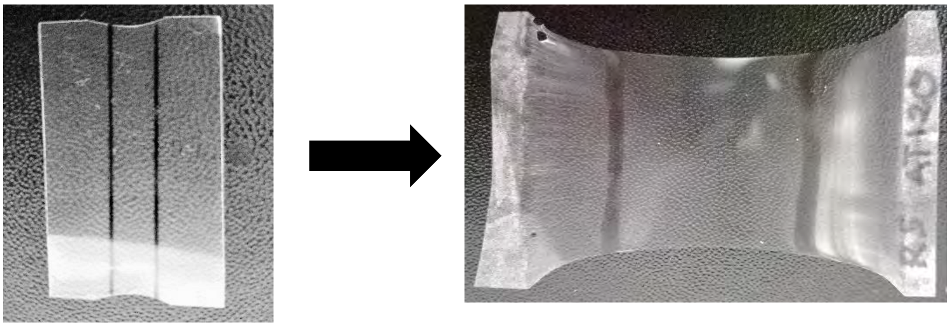

Before drawing

After drawing

Figure 3.1: The PLLA film before and after drawing at ratio 5

A metal holder with a rough surface was used to clamp the film on both sides. The clamp was carefully tightened to prevent the films from slipping out of the holder during the drawing motion. At a constant temperature of 80°C, the films were drawn in ratios of 2, 3, 4, 5, and 6. Figure 3.2 illustrates the experimental setup for the uniaxial drawing process. A hot air gun was employed to keep the film surface heated. The PLLA film becomes exceedingly brittle below the glass transition temperature ($T_{g\sim}$ 75°C), hence the drawing temperature above T_g which is 80°C was applied in this study. Following the drawing procedure, the film was annealed for one hour at various temperatures (80 °C, 100 °C, 120 °C, 140 °C, and 160 °C). The film was restrained in the metallic holder during the annealing process to prevent it from returning to its original position. Subsequently, the thickness of the film was determined using a micrometer screw gauge.

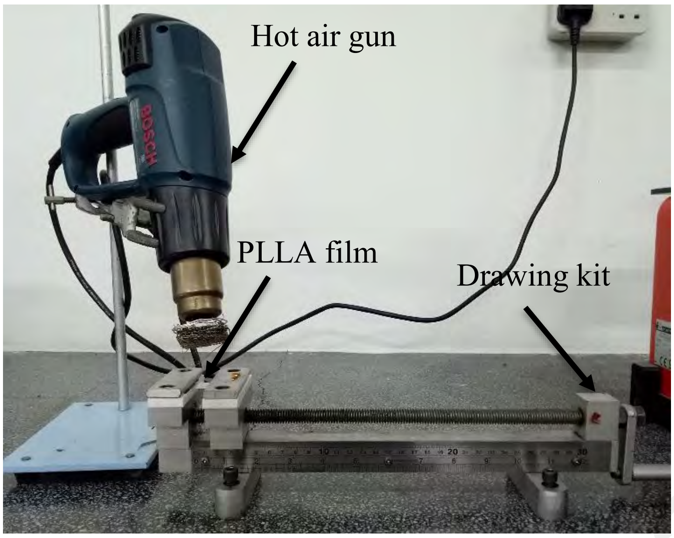

Figure 3.2: The drawing process

3.3 Cutting the PLLA film

The elongated films were deposited with aluminium (Al) electrodes on both sides for electrical (dielectric and piezoelectric) measurements. The Al deposition was carried out in a glove box with a nitrogen gas atmosphere using a thermal evaporator. As depicted in Figure 3.3, rectangular or square pieces were cut from the films at a 45° angle to the orientation direction. Because we are examining the shear piezoelectricity of the PLLA film, it is vital to cut the sample this angle. A microscope and a micrometer screw gauge were used to determine the effective electrode area and thickness of the films, respectively.

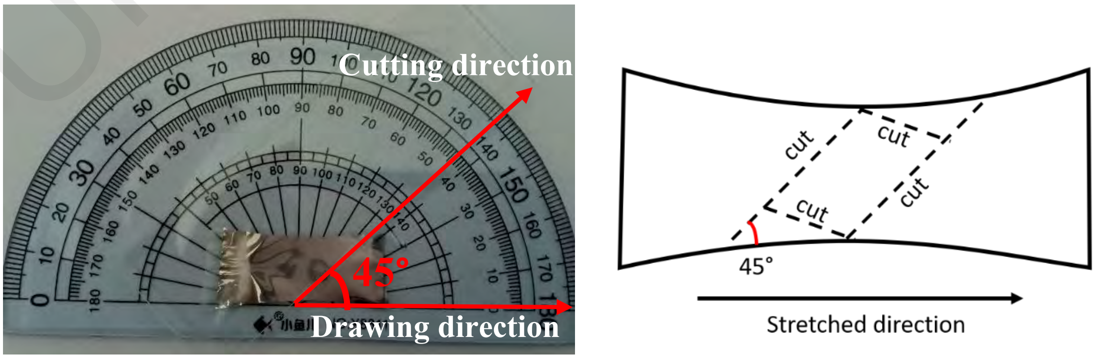

Figure 3.3: The 45^o cutting angle of the elongated PLLA film

3.4 Characterization

3.4.1 Differential Scanning Calorimetry (DSC)

The differential scanning calorimetry (DSC) is a thermal analytical technique that detects the difference in the heat flow of the sample and reference as a function of temperature. The DSC configuration is depicted in Figure 3.4. The DSC system is composed of three basic components: a source of heat (the furnace), a source of measurement (thermocouples), and controls (software). The furnace is made of a highly conductive metal, such as silver which encloses the DSC head, forming a chamber that is aided by a continuous nitrogen flow. Heat is delivered to the furnace at a linear rate until temperature differences (ΔT) between the sample thermocouple (T_S) and reference thermocouple (T_R) are recorded. After dividing the temperature difference, ($\Delta T_{SR} = T_S - T_R$) by the thermal resistance of the system, R_{th}, and applying a calibration factor, k the temperature variations, ΔT_{SR} are converted to a DSC signal (Φ). After that, the DSC signal is either plotted against temperature or time to form a DSC curve.

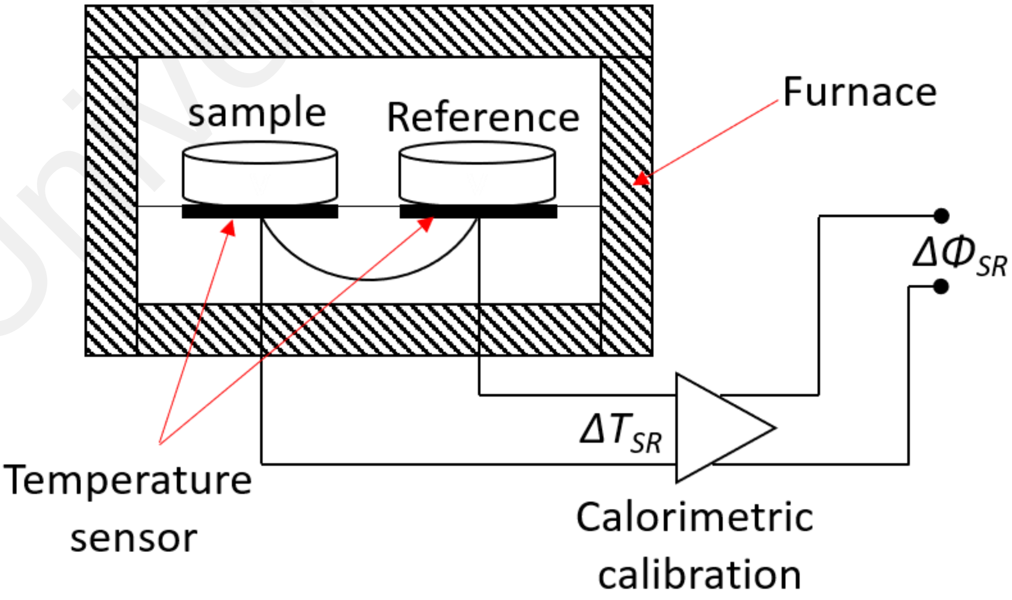

Figure 3.4: The illustration of DSC. Adapted from (Hemminger & Sarge, 1998)

From the DSC plot (see Figure 3.5), the glass transition temperature, T_g, crystalline melting temperature, T_m and the percentage of crystallinity, X_c were determined. The T_g is the temperature at which a stiff glassy material transforms into a soft (non-melted) material. The T_m is the melting temperature of the crystalline domains in PLLA.

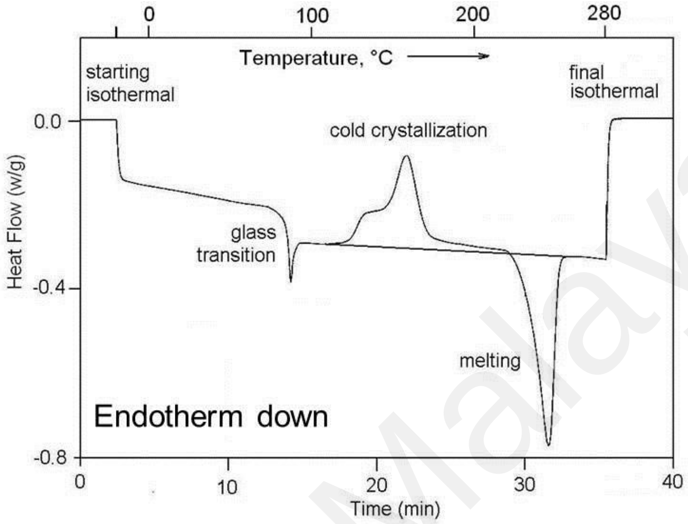

Figure 3.5: The DSC curve for poly(ethylene terephthalate), PET. Photo sourced from (Gotro, 2014)

DSC was performed using a Mettler-Toledo DSC822e machine calibrated with an indium standard. For sub-ambient temperature, an intercooler (HAAKE EK/90 MT) was employed. To begin, the PLLA sample was sealed in a shallow aluminium pan (~4 mg), and an empty crucible was utilized as a control. In this experiment, two heating and cooling cycles have been set. The first cycle's goal was to erase the thermal history. On the second heating, the T_g and T_m were measured. The first cycle began at 25°C and progressed to 200°C at a rate of 10°C/min, then was held at that temperature for one minute before being air cooled to 25°C at a rate of 10°C/min. For the second cycle, the same temperature trend was repeated. The collected data was analyzed using the STAR program. The crystallinity percentage, X_c was calculated using the following equations:

$$X_c = \frac{\Delta H_m - \Delta H_c}{\Delta H_m^{\circ}} . 100\% \tag{3.11}$$

where ΔH_m is the melting heat, ΔH_c is the cold crystallization heat determined by integrating area under the peaks in J/g. The ΔH_m° is the melting heat for 100% crystalline PLLA which is 93.1J/g (Sosnowski, 2001).

3.4.2 Wide Angle X-Ray Scattering (WAXS)

The Wide-Angle X-Ray Scattering (WAXS) spectra of the samples were collected using synchrotron radiation at Beamline 1.3 Synchrotron Light Research Institute (SLRI), Thailand. The setup is shown in Figure 3.6. A double multilayer monochromator was adopted to monochromatize synchrotron X-rays within 9 keV energy. Sample is attached to the metal frame with a square aperture of 10 x 10 mm^2 to the sample stage and the measurement is performed in room temperature. The sample-to-detector distance was ~214.3 mm.

WAXS works by directing monochromatic X-ray beams onto a sample, where they are scattered by unique filtrations of electron density within the material. After passing through a vacuum tube, the scattered intensity was detected by a 2D CCD detector.

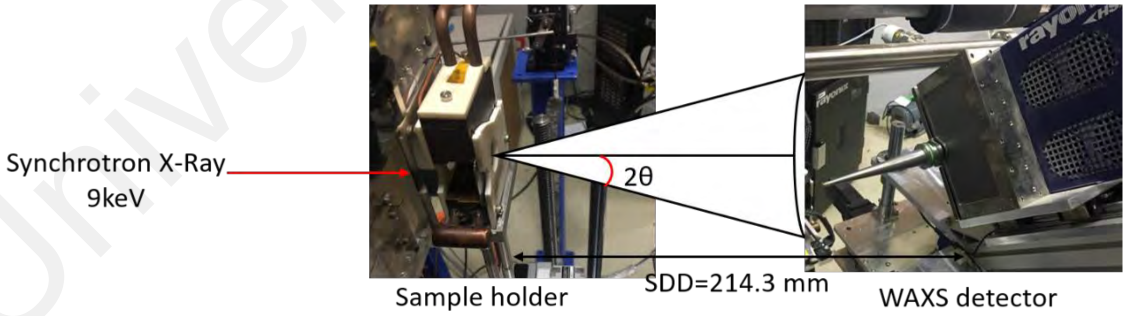

Figure 3.6: The WAXS setup at Beamline 1.3 SLRI

Scattering intensity (I) over a range of scattering vector magnitudes (q) (I versus q) or two-dimensional (2D) scattering intensity maps were used to depict the WAXS profile. SAXSIT software was used to transform I vs q to I vs 2θ for further analysis.

A Cartesian coordinate system (*XYZ*) was assigned to the polymer, with the *Z*-axis parallel to the orientation direction, and each crystallite a Cartesian coordinate system ($X^cY^cZ^c$), with the Z^C axis as the crystallite's orientation axis. As shown in Figure 3.7(a), Euler angles (χ, ψ, ω) are used to characterise the crystallite's orientation. X-ray diffraction was used to determine the orientation factor, F_c of the *c*-axis. The dependence of the diffraction intensity, *I*, on the rotation angle of the sample was determined using the symmetrical transmission technique described in Figure 3.7(b). $I(\chi)$ gives the orientation distribution of plane normal (Krigbaum & Roe, 1964) that is parallel to the sample plane and corresponds to the Bragg angle 2θ. The χ is the angle between the plane connecting the incident and diffracted beams and the plane containing the fiber axis and the bisector of the external angle formed by the two beams (see Figure 3.7b). The orientation factor, F_c is determined using $I_c(\chi)$, which is related to the diffraction plane perpendicular to the *c*-axis, if the sample is uniaxially oriented. The F_c is given as

$$F_c = \frac{3\langle \cos^2 \chi_{c,Z} \rangle - 1}{2} \tag{3.12}$$

where $\langle \cos^2 \chi_{c,Z} \rangle$ is the average cosine value calculated between the polymer chain axis, (*c*-axis), and the sample draw direction, *z*-axis, assuming that the orientation is uniaxial. We evaluated the $\langle \cos^2 \chi_{c,Z} \rangle$ of the oriented PLLA film using the diffracting plane (110/200) via the equation below

$$\langle \cos^2 \chi_{c,Z} \rangle = \frac{\int_0^{\pi} I_{hkl}(\chi) \cdot \cos^2\chi \cdot \sin\chi \cdot d\chi}{\int_0^{\pi} I_{hkl}(\chi) \cdot \sin\chi \cdot d\chi} \tag{3.13}$$

where $I_{hkl}(\chi)$ is the scattered intensity of (110/200) reflection at the χ angle. The strong (110/200) plane diffraction was measured at 2θ=16.5°. The (110/200) plane is perpendicular to the *c*-axis, thus $I_c(\chi)$ is related to $I_{(110\,/\,200)}(\chi)$ by

$$I_c(\chi) = I_{(110/200)}(\chi - \tfrac{\pi}{2}) \tag{3.14}$$

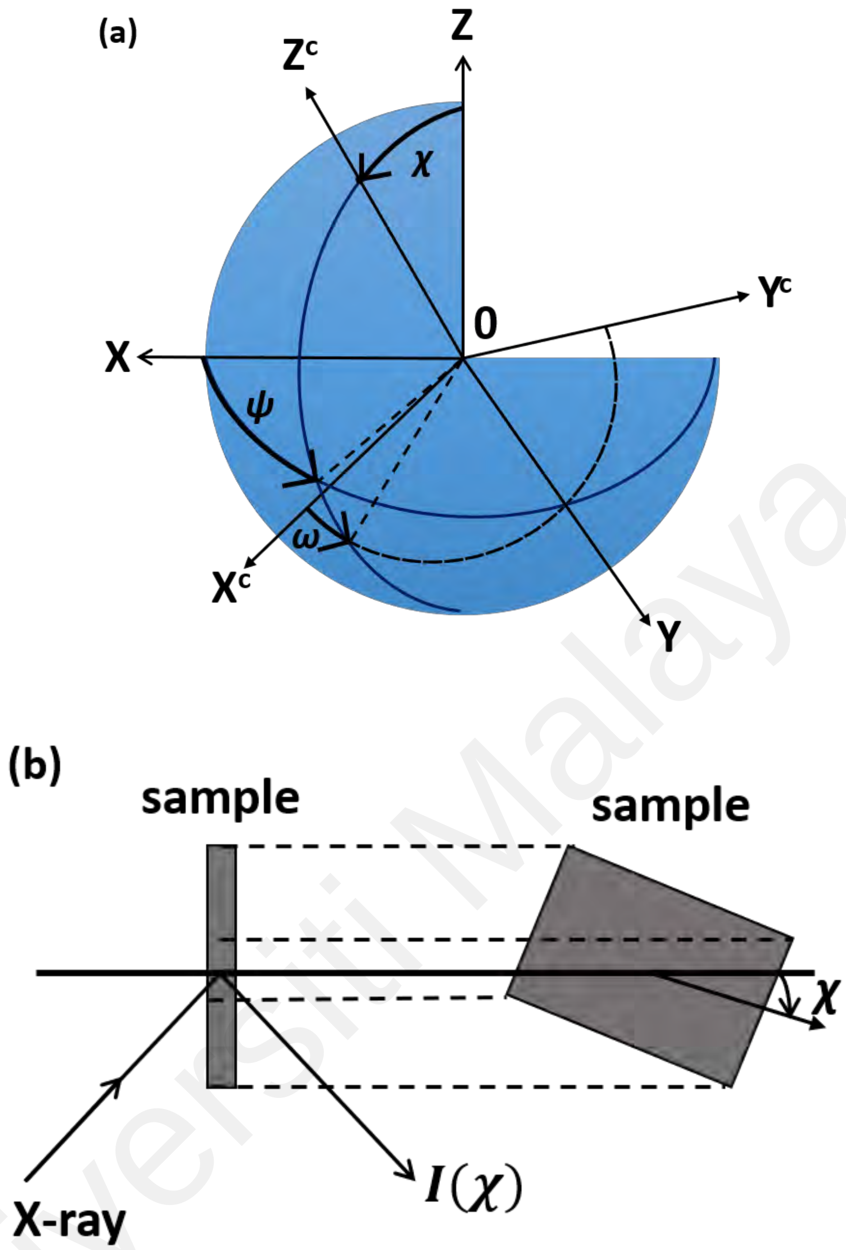

Figure 3.7: Cartesian coordinate systems utilized to characterize a crystallite's orientation. The Z-axis is the film's orientation direction, while the Z^c-axis is the crystallite's orientation axis (the c-axis). (b) The technique of symmetrical transmission is used to measure $I(\chi)$. Adapted from (Takeo Furukawa & Fukada, 1976)

3.5 Electrical Measurements

3.5.1 Dielectric & piezoelectric measurements

Agilent 4294-A Precision Impedance Analyzer was used to determine the real dielectric permittivity, *ε'* and imaginary dielectric permittivity, *ε"* of PLLA. Capacitance, *Cp*, and tan *δ* were measured between 40 Hz and 15 MHz at temperatures ranging from 25°C to 140°C in 5°C increments. The *Cp*, and tan *δ* were then converted to *ε'* and *ε"*, respectively. To establish electrical contact, silver paste was used to attach aluminium wires to both surfaces of the aluminium coated PLLA material. Subsequently, the sample was placed into a cryostat. A Lakeshore 335 Temperature Controller was used to regulate the temperature. Figure 3.8 illustrates the experimental setup for dielectric. The values of C_p and tan *δ* could then be computed concurrently. The complex permittivity, *ε'* and *ε"* was computed using equation 3.15 and 3.16 respectively.

$$\varepsilon' = \frac{C_p t}{\varepsilon_0 A} \tag{3.15}$$

where, ε_0 is the vacuum permittivity which is 8.85×10^{-12} F/m

A is the electrode area on the PLLA film in m^2

t is the thickness of the PLLA film in m

The imaginary part of permittivity, *ε"* is determined using equation 3.16.

$$\varepsilon" = \varepsilon'.tan\delta \tag{3.16}$$

where, tan *δ* is the dissipation factor

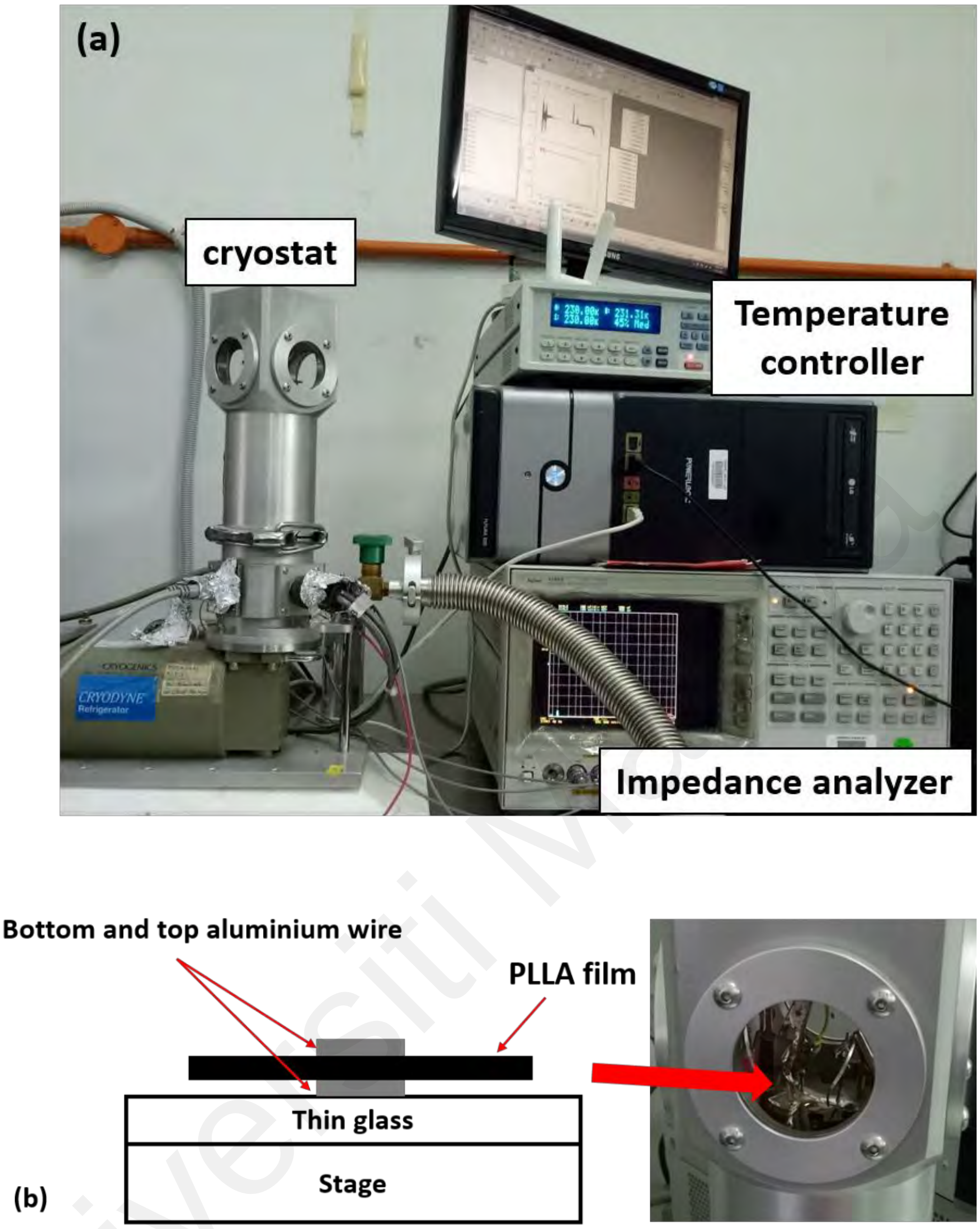

Figure 3.8: (a) The dielectric measurement setup and (b) the setup of the sample inside the cryostat

We fitted the dielectric relaxation of PLLA using the Havriliak and Negami (HN-function) (see Eq. (2.26)) utilizing the IGOR Pro Software, adjusting the HN function's fitting parameters such as α, β and $\Delta\varepsilon$ so that it fit the experimental data. Additionally, the resonance peaks for the drawn films were fitted using the same approach but we also incorporated the length extension (LE) mode (see Section 2.5.5 for further detail on the

LE mode) in the procedure file. The compliance, s, and complex electromechanical coupling factor along the length direction, k_l, were determined by fitting the experimental result. Finally, using equation 2.61, the piezoelectric constants d_{14} and e_{14} are calculated.

CHAPTER 4: RESULTS AND DISCUSSION

4.1 Introduction

This chapter addresses the analysis of experimental results and pertinent discussions. In section 4.2.1, the results of wide-angle X-ray scattering (WAXS) for non-drawn samples at various annealing temperatures are presented, followed by the results for drawn samples at various annealing temperatures in section 4.2.2. The crystallinity percentage and orientation factor of the PLLA samples were also discussed here. Section 4.3 compares the thermal properties of all PLLA samples, while Section 4.4 discusses the dielectric relaxation, including its origin and behaviour. In Section 4.5, piezoelectric relaxation and the model used to study the relationship between amorphous and crystalline regions are presented and discussed in greater detail. In section 4.6, the relationship between piezoelectricity, crystallinity, and orientation is described.

4.2 Wide Angle X-ray Scattering (WAXS)

Wide Angle X-Ray Scattering is a powerful technique used to comprehend the effects of orientation on the crystalline structure of semi crystalline PLLA. WAXS also offers information about the structural changes that happened in the amorphous and crystalline regions as a result of uniaxial deformation. The 2D WAXS images can be used to qualitatively measure the molecular chain orientation of the samples. In the following sections, the WAXS results obtained for biaxial PLLA film will be discussed.

4.2.1 Non-drawn PLLA films

Figure 4.1 depicts 2D-WAXS images and 1D-WAXS profiles as a function of annealing temperatures for the non-drawn samples. For non-annealed films, the WAXS pattern displays very low intensity of Debye-Scherrer rings. The rings get more intense at (200,110) and the (203) planes when the film annealed at 80 °C, and the intensity increases as we anneal at 160 °C. The strongest reflection planes are (200,110) and (203), implying that PLLAs are randomly oriented α crystals (Alemán et al., 2001). Figure 4.1 depicts a comparison of the related 1D-WAXS profiles. The (103), (010), (200,110), (203), and (210) planes have five separate diffraction peaks at the 2θ = 12.3°, 14.6°, 16.5°, 18.9°, and 22.2°, respectively (Kawai et al., 2007; Pan et al., 2007; Zhang et al., 2004). The intensity of the scattering planes grew as the annealing temperature increases, showing that the materials' crystallinity increased.

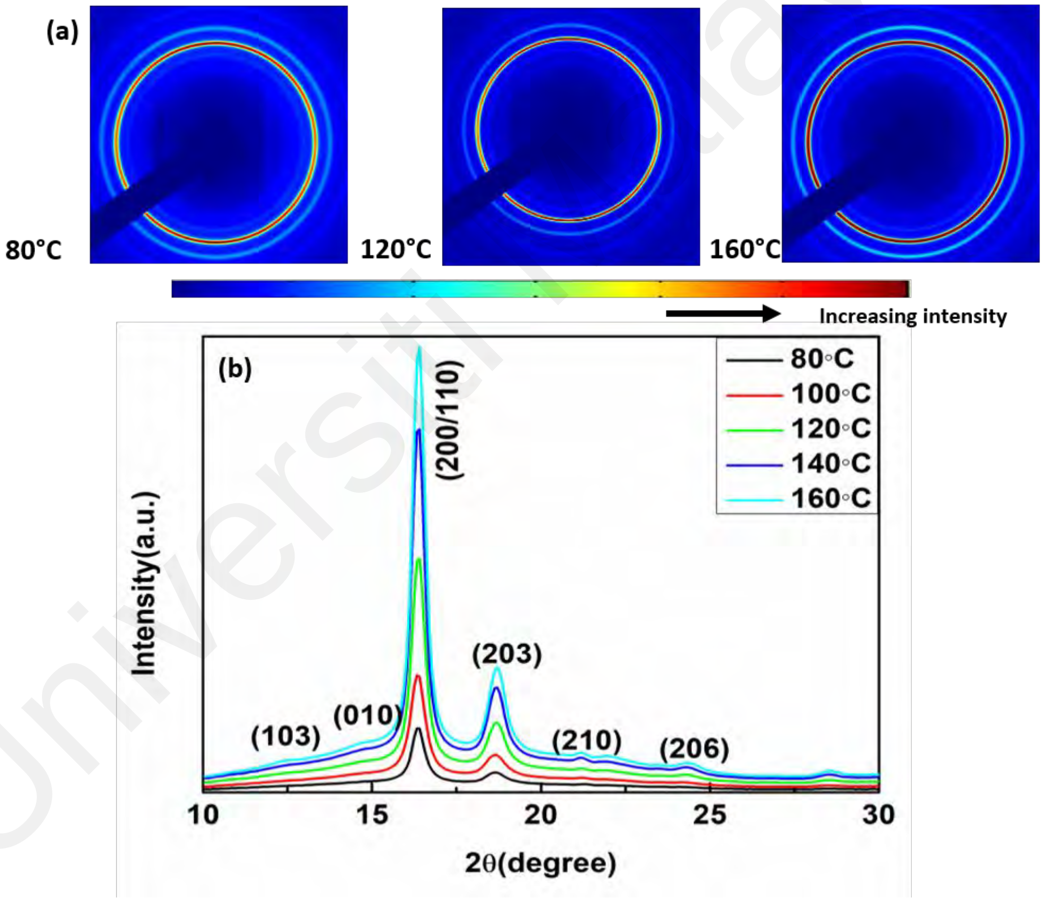

Figure 4.1: (a) 2D WAXS image and (b) 1D WAXS profile for nondrawn sample annealed from 80 °C to 160 °C.

For quantitative analysis, the crystalline and amorphous regions were deconvoluted using a combination of Gaussian and Lorentz functions. Neat PLLA film (non-drawn or annealed) was used to determine the amorphous peak (refer to Fig. 4.2(a)). The amorphous peak is represented by the broad peak below the crystalline peak. Both peaks were fitted with a Gaussian function. The percentage of crystallinity, X_c was then evaluated from the ratio of the crystalline area over the total area under the diffraction curves of amorphous and crystalline regions. Figure 4.2 (a) shows the typical deconvolution of the crystalline and amorphous peak of the PLLA, while Figure 4.2 (b) present the percentage of crystallinity, X_c for the non-drawn film annealed at various temperatures. The amorphous peak was determined. The results show that as the annealing temperature is raised from 80 °C to 160 °C, the degree of crystallinity increases from 34 % to 57 %.

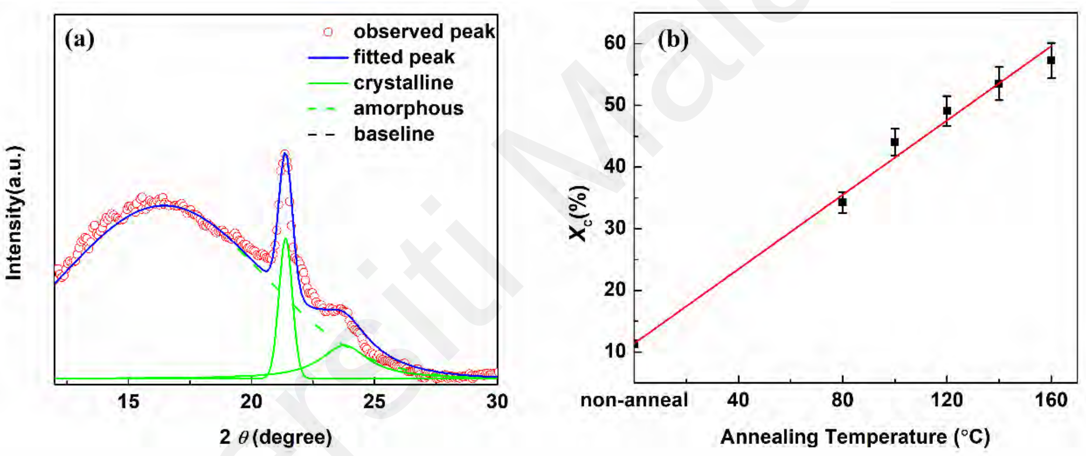

Figure 4.2: (a) The plot illustrates deconvolution of the WAXS plot in the PLLA film (non- drawn and annealed). (b) The plot displays the evaluated percentage of crystallinity, X_c of the neat (non-drawn and non-annealed) and non-drawn film annealed at 80 °C, 100 °C, 120 °C, 140 °C and 160 °C.

4.2.2 Uniaxially drawn PLLA films

To investigate the orientation effect and the crystallinity, the PLLA samples were drawn at different drawing ratios, λ (2, 3, 4, 5, 6) and annealed at different temperatures (i.e., 80 °C, 100 °C, 120 °C, 140 °C, and 160 °C), respectively. The WAXS results are shown in Figure 4.3 where 4.3 (a) depicts the changes in the 2D WAXS image as a result of sample annealing at 160 °C with a varied drawing ratios, λ. Drawing to λ =2, a progressive transition from isotropic diffraction to a narrow arc-like ring can be seen for the strongest (200/110) plane reflection of α-PLLA crystal, indicating that initially the crystal was somewhat orientated along the shear direction (Ru et al., 2016). The dispersion of azimuthal angle at the (200/110) diffraction arcs reduced as the λ increases, and more *hkl* peaks were seen. The addition of more crystalline peaks indicates the increase of crystallinity. Furthermore, when the drawing ratio increases, the ring becomes narrower and more intense, suggesting that the orientation and crystallite perfection are emerging within the sample (Heeley et al., 2020). It is clear that the annealing temperature has an effect on the ring intensity. The intensity shifts are plainly apparent in the 1D WAXS profile displayed in Figure 4.3 (c).

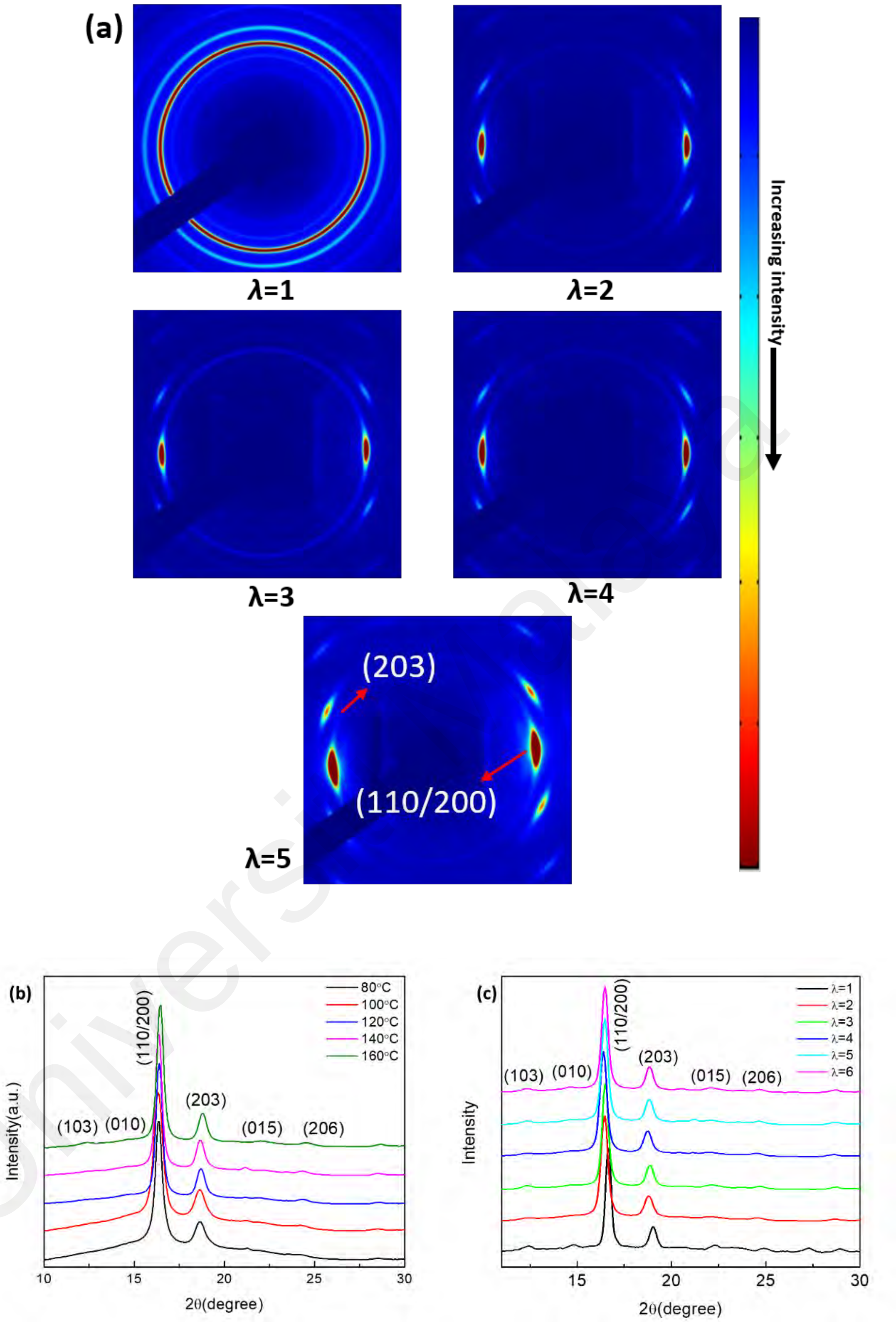

Figure 4.3: (a) 2D WAXS images for various drawing ratio samples annealed at 160°C, (b) 1D WAXS profile for λ=2 annealed at different temperature, (c) 1D WAXS profile for different drawing ratio sample annealed at 160 °C.

Figure 4.4(a) to (d) depicts the deconvolution graph for λ=2 and λ=6 annealed at T_a=80 °C and T_a=160 °C while Figure 4.4(e) represent the percentage of crystallinity, X_c, of all samples. The graph shows that the film annealed at 160°C has the highest X_c, regardless of drawing ratio. The maximum X_c was obtained from the film drawn at Ratio 6 and annealed at 160°C, which is ~85%. Figure 4.4(d) shows how the amorphous halo peak (shown by the dashed green line) reduce tremendously as the film drawn to λ=6 and annealed at T_a=160°C. The results indicate that the increase of crystallinity is because the amorphous regions become more oriented during the drawing and annealing process.

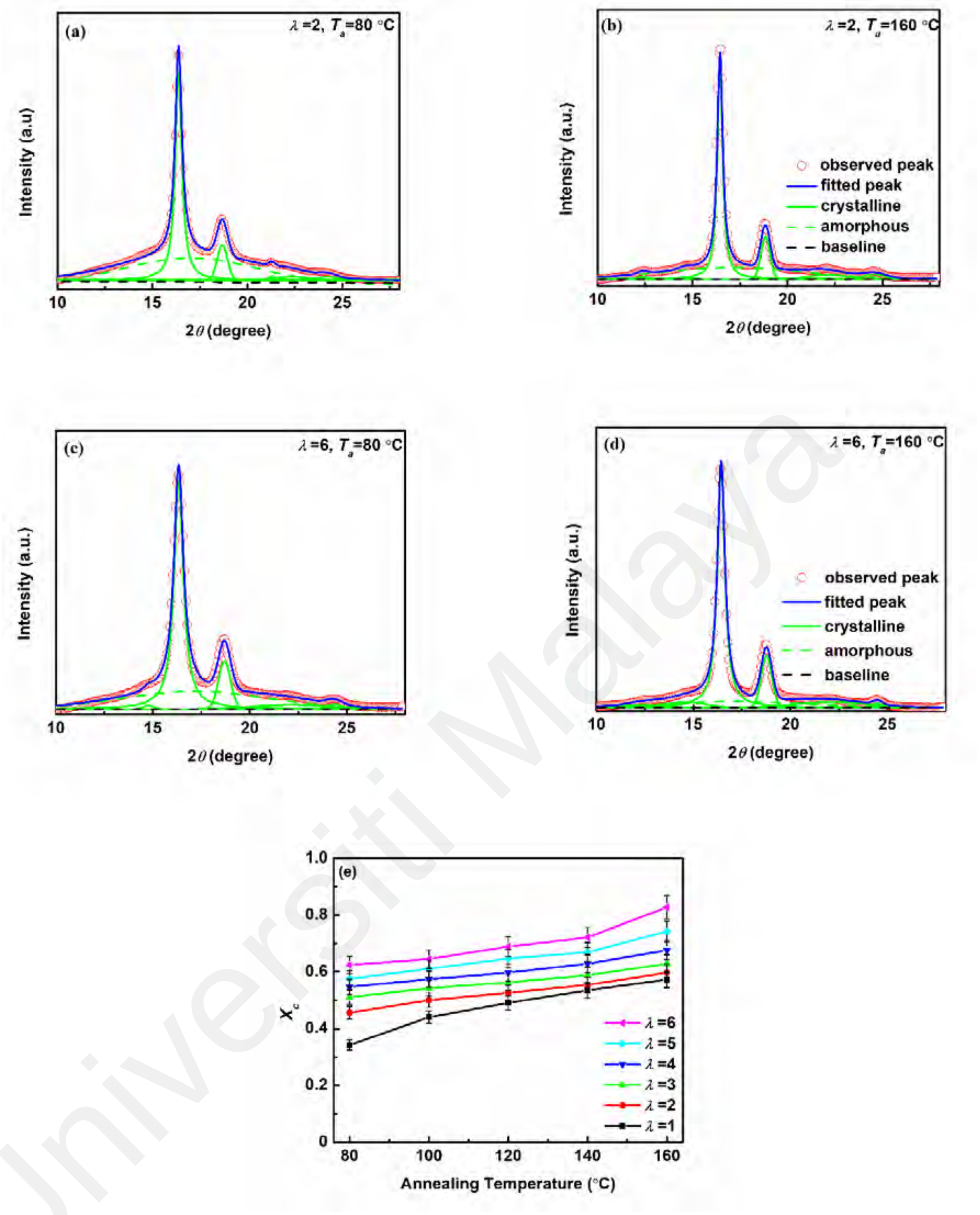

Figure 4.4: X-ray diffraction patterns and their crystalline and amorphous peak deconvolution curves for samples (a) λ=2; T_a = 80 °C, (b) λ=2; T_a = 160 °C, (c) λ=6; T_a =80 °C, (d) λ=6; T_a =160 °C. Fig 4.4 (e) shows the degree of crystallinity, X_c versus annealing temperatures for various drawing ratios.

From the diffraction pattern (200/110) planes of the α form PLLA, the crystallite orientation factor, F_c was calculated using Equation (3.12) for all the samples and shown in Figure 4.5. The non-drawn films (λ=1) are randomly oriented, and the annealing temperature has no influence on the F_c. On the other hand, with stretched PLLA film, annealing temperature has a significant impact on the molecular orientation. The F_c increased as the draw ratio and annealing temperature were raised. Since the samples were annealed in the restrained manner in the holder (at the elongated length), it was possible that the PLLA crystal continue to orient slowly during the annealing process. This is proven by a small change in the length of the film following the annealing process.

The computed F_c coincides with Tanaka & Young (2006) result, in which the F_c rapidly increases from λ=1 to λ=2. Figure 4.6 depicts their proposed deformation model for this phenomenon. Shear tension in the lamellae structure is formed during drawing as a result of longitudinal tensile stress. When drawing, the crystallite rotates to reduce shear stress while the amorphous zone elongates, promoting a rapid increase in the orientation from λ=1 to λ=2.

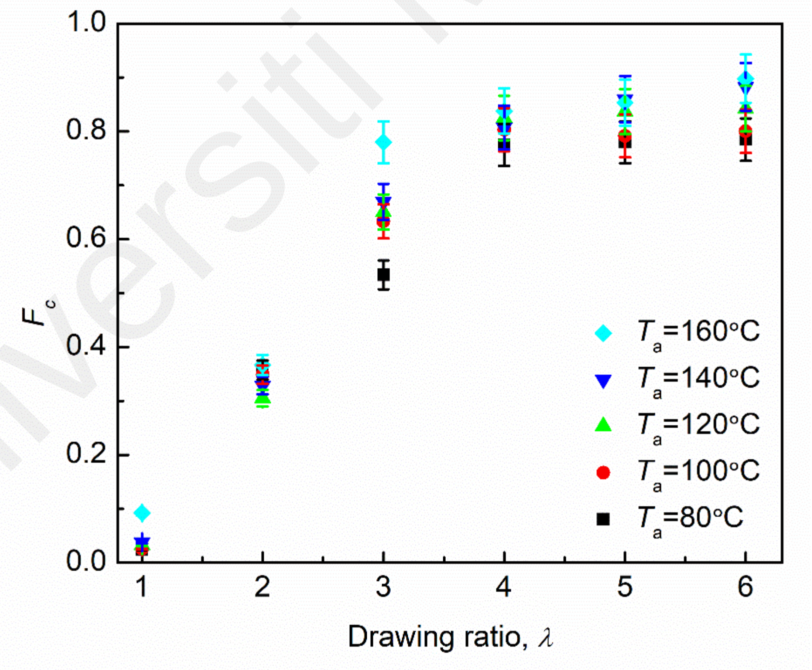

Figure 4.5: Changes of F_c as a function of annealing temperature and drawing ratio.

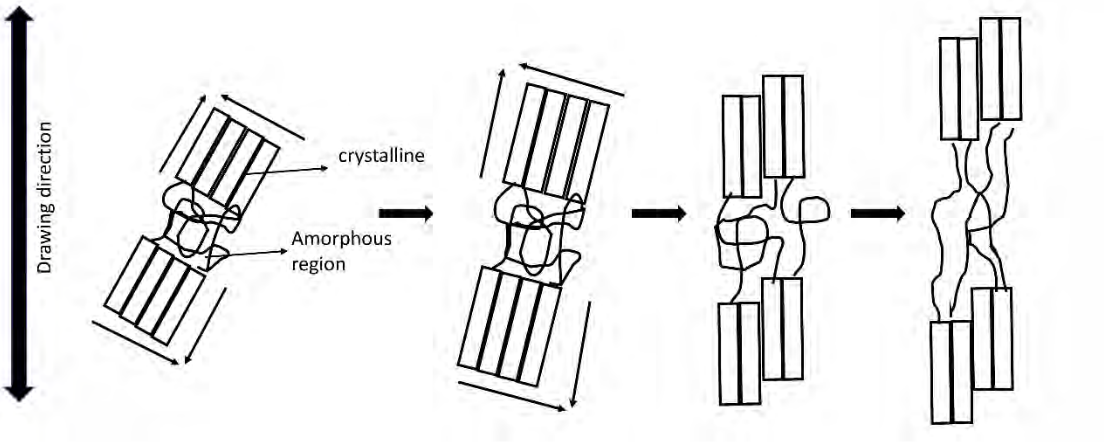

Figure 4.6: Deformation model for crystallites and amorphous region during uniaxial drawing. Adapted from (Tanaka & Young, 2006).

4.3 Differential Scanning Calorimetry (DSC)

In Figure 4.7(a) and (b), the overlay thermograms of non-drawn samples annealed at various annealing temperatures and samples drawn at various drawing ratios are shown, while Table 4.1 summarises the thermal characteristics and X_c. The glass transition temperature, T_g of non-annealed and annealed samples are nearly identical, indicating that annealing had little effect on the T_g. For non-annealed sample, an obvious crystallization temperature, T_c can be observed due to crystalline structure is generated during heating cycle. The change of annealing temperature and draw ratio have a significant change on the T_c as shown in Figure 4.7 (a) and (b), where the T_{c} is not observable. This indicates that a high crystal content was formed during the annealing and drawing process, therefore not much new crystalline structures were generated during heating cycle.

The existence of small endothermic peak just prior to the melting peak can be observed for annealed sample originating from the transition of disorder α' to more ordered α-form (Barkhad et al., 2020). At T_{a}=160 °C and increasing drawing ratios, the peak disappear due to the strain-induced molecular orientation limits the transition of α' to α form during the heating scans. The melting temperature, T_m shifts to a higher temperature as the annealing temperature increases maybe due to the change of crystal morphology of PLLA. The drawn sample exhibits a decrease in melting temperature. This is possibly because stretching reduces the lamellae thickness, consequently lowering the melting point which it become easier to transform into liquid.

Table 4.1 and Table 4.2 show the percentage of crystallinity, X_c, of the samples computed from DSC results. In comparison to the WAXS, both X_c data exhibit a similar growing trend corresponding to the annealing temperatures. However, the X_c values determined by DSC were typically lower than those determined by WAXS as reported by the reference (Kong & Hay, 2002, 2003). The WAXS measurement focused on the sample's surface, thereby concentrating on the material's crystallites. As a result, processing conditions such as strain-induced orientation and sample’s surface cooling have a significant effect on it. In contrast, the DSC measurement determines the degree of crystallinity using the enthalpy of heating a bulk sample. During the annealing process, a strain-induced crystallization occurs. Region with smaller crystal relaxed prior to the melting point, impacting the crystallinity of the material (Dillon et al., 2019).

Table 4.1: The glass transition temperature (T_g), melting temperature (T_m), enthalpy of cold crystallization (ΔH_c) and enthalpy of melting (ΔH_f) of the non-drawn sample measured at different annealing temperatures.

Annealing Temperature (°C)	T_g (°C)	T_c (°C)	ΔH_c (J/g)	T_m (°C)	ΔH_m (J/g)	X_c (%)
Non-annealed	56.7	86.7	25.2	165.7	38.1	14
80	55.7	-	-	165.0	38.5	41.1
100	56	-	-	165.7	38.3	41.3
160	55	-	-	167.7	42.1	45.0

Table 4.2: The glass transition temperature (T_g), melting temperature (T_m), enthalpy of cold crystallization (ΔH_c) and enthalpy of melting (ΔH_f) of the PLLA samples drawn at various ratios and annealed at 160 °C.

Drawing ratios, λ	**T_g (°C)**	**T_m (°C)**	**ΔH_f (J/g)**	**X_c (%)**
2	56.0	161.3	42.2	45.3
3	55.7	162.3	43.1	46.3
5	56.7	164.3	44.0	47.3
6	56.0	164.7	44.1	47.4

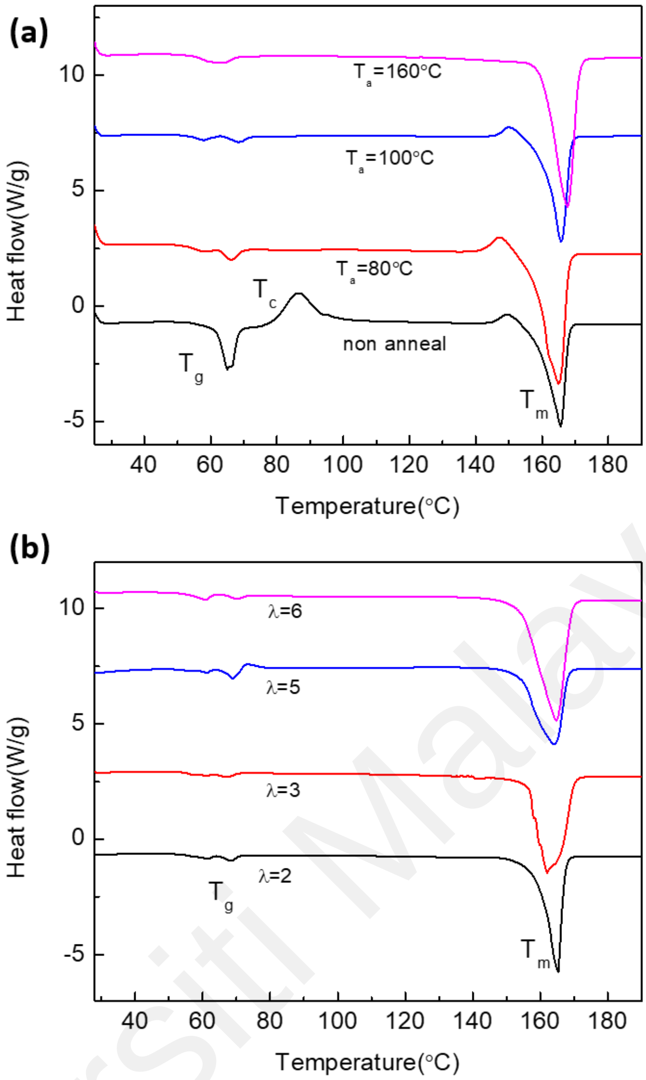

Figure 4.7: DSC thermograms plot of the samples (a) annealed at various temperatures and (b) uniaxially drawn at various drawing ratios and annealed at 160 °C.

4.4 Dielectric relaxation spectroscopy

Figure 4.8 shows the complex permittivity (real permittivity, ε' and imaginary permittivity, ε'') of the neat untreated (Figure 4.8a) and drawn at drawing ratio, λ=6 and annealed at T_a=160 °C (Figure 4.8b) PLLA films as a function of frequency and temperatures, respectively. The real permittivity, ε' increased with increasing temperature while distinct relaxations are observed from the ε'' spectrum.

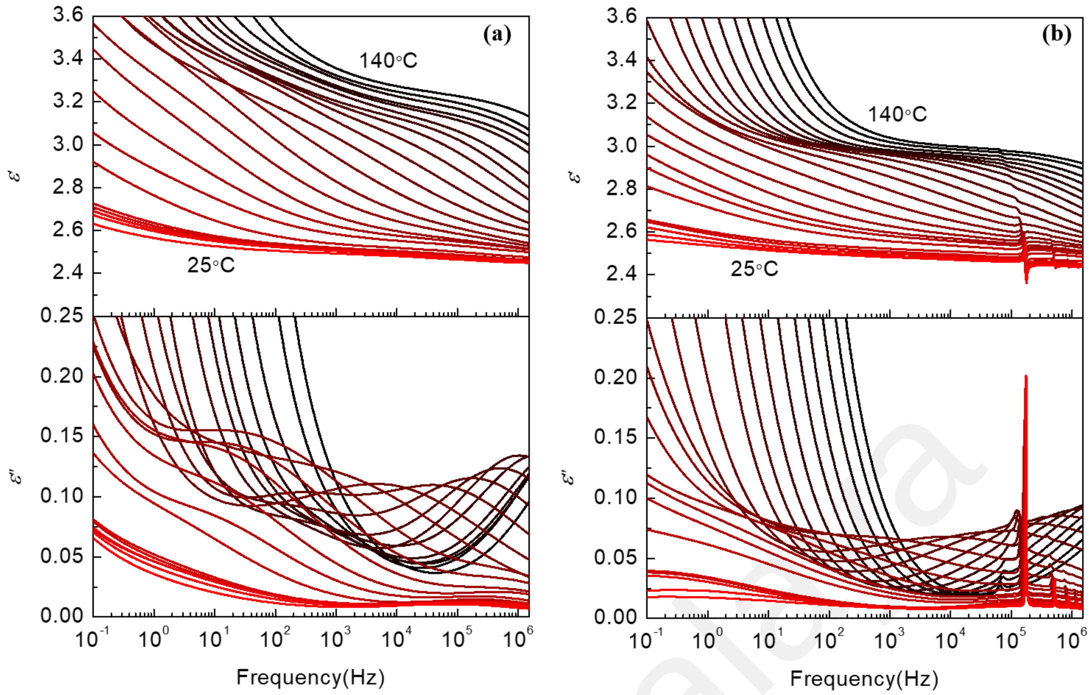

Figure 4.8: Complex permittivity of PLLA heating from 25 °C to 140 °C with a temperature step of 5 °C for (a) neat film (amorphous sample) (b) uniaxially drawn, λ =6 and annealed at 160 °C (highly oriented and crystalline sample).

The neat film (low crystallinity) and the uniaxially drawn film (highly oriented and crystalline) were used to study the effect of the crystallinity on the dielectric relaxation. For both type of films, a broad relaxation is observed in the imaginary permittivity above 70 °C (above the glass transition temperature, T_g) which is related to the segmental dynamics and shifted to higher frequencies as the temperature increased. The obvious difference between both samples is the maximum dielectric loss peak decrease with increasing crystallinity. This is attribute to the reduce of amorphous region where the segmental relaxation occurs and also due to the restriction of dipolar orientation in crystalline regions (Hikosaka et al., 2011). The reduction of dielectric loss peak could be observed later from the calculated dielectric strength. On the other hand, the local β-relaxation occurs at low temperature which is below T_g which is attributed to localized motion of side methyl group rotating perpendicular to the backbone (Kanchanasopa & Runt, 2004; Mierzwa et al., 2002). Nearing to T_g, the β-relaxation coincided with the α-

relaxation. In addition to the molecular relaxation, the dielectric spectra exhibit sharp resonance peaks at ~200 kHz for the oriented samples (see Figure 4.8b) which is not discernible in the non-drawn samples. The appearance of resonant peak indicates the occurrence of piezoelectric effect in the film. The resonance peak will be used later to calculate the piezoelectric constant. The high values of *ε'* for non-treated film at low frequencies may be due to the presence of space charge polarizations that occur at the electrode and its low value at high frequencies may be due to the loss of significance of these polarizations gradually.

The Havriliak-Negami equation, presented in Eq. 2.26, is a regularly used fitting function to quantify the dielectric strength ($\Delta\varepsilon$) and relaxation time (τ), for both segmental and local relaxations, as explained in detail in the section 2.2 (Wübbenhorst & Turnhout, 2012).;

$$\varepsilon^* = \varepsilon_\infty + \frac{\Delta\varepsilon}{[1+(i\omega\tau_i)^{\alpha_{HN}}]^{\beta_{HN}}} \tag{2.26}$$

where the Δε is the dielectric strength, $\tau_i = 1/2\pi f_i$ is the relaxation time and the exponent α_{HN} and β_{HN} are the distribution parameters. The β_{HN} describe the symmetry shape parameter which range from value 0 to 1. Crystalline polymers have been widely shown that it displays a symmetric α-relaxation (Coburn & Boyd, 1986). Therefore, a value 1 for β_{HN} parameter was used to fit the HN function of highly oriented and crystalline sample. Contrary, the amorphous polymer have asymmetric α-relaxation, therefore the β_{HN} was kept at a constant value of 0.5 for all temperature while changing the α_{HN} (Kanchanasopa & Runt, 2004) . The α_{HN} describes the peak breadth shape parameter which range from 0 to 1 to depict the narrowness of the relaxation (Wübbenhorst & Turnhout, 2012). As discussed in section 2.5.5, the resonance will be fitted using the LE mode equation (Eq. 2.61). As the resonance frequencies lie in the vicinity of the molecular relaxations, it is necessary to include the contribution of dielectric relaxation during the analysis of the spectra.

The exemplary fitting of the piezo resonance and dielectric relaxation (using Eq. 2.26 & Eq. 2.61) is shown in Figure 4.9.

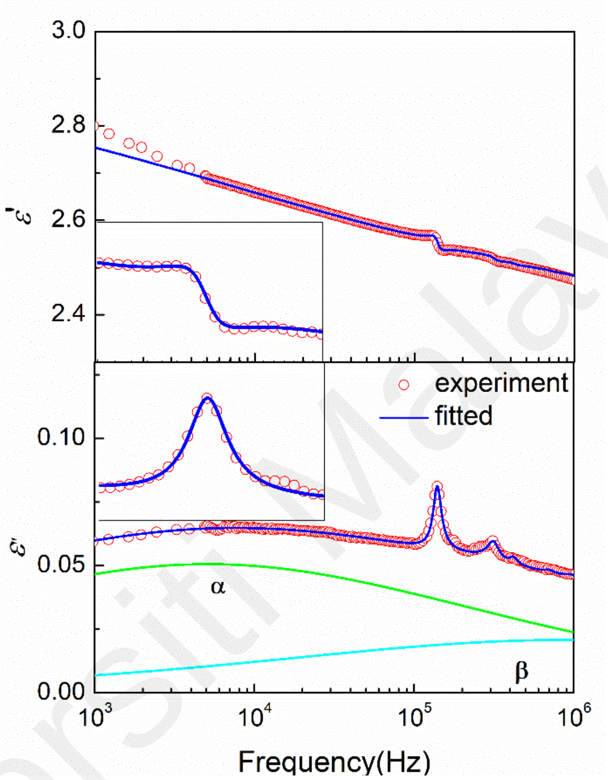

Figure 4.9: The exemplary fitting of the piezo resonance and dielectric relaxation of PLLA measured at 90 °C.

Now we discussed the origin of the dielectric relaxations in the PLLA samples. We observed two relaxations for both amorphous (untreated samples) and highly crystalline and oriented PLLA samples; α- and sub-glass β-relaxation. The exemplary curve fitting of the processes is shown in Figure 4.9. The α-relaxation in PLLA is associated with the dipolar fluctuations from the segmental motions along the chain backbone and identified as mobile amorphous phase in between the crystalline lamellae (Dionísio et al., 2005; Jindong Ren & Adachi, 2003). On the other hand, the sub-glass β-relaxation at higher frequencies attributed to the local twisting motion of the main chains (Dionísio et al., 2005; Jindong Ren & Adachi, 2003). Figure 4.10 (a) shows the dielectric strength of both processes as a function of temperature for the neat film (amorphous), heat-treated film (highly semicrystalline) and drawn and heat-treated, λ=6, T_a=160 °C film (highly oriented), respectively. The dielectric strength of the β-relaxation and α-relaxation significantly reduced from the amorphous to semicrystalline and oriented PLLA, indicating that dipolar fluctuations from the segmental motions along the chain backbone and the twisting motion of the main chain are restricted in highly crystalline and oriented films. It is also apparent that the orientation has less effects on the molecular motion compared to the crystallinity effects. The amount of relaxing material is continually reduced by crystal formation due to the progressive transfer of a percentage of the amorphous material to the developing crystalline phase that can also be observed in the WAXS measurement, where the amorphous decreases with the increase of crystallinity. In amorphous PLLA, all the conformational motion occurs in the bulk-like amorphous phase while for fully semi-crystalline PLLA, all the amorphous phase exist within the spherulites, constrained between the crystalline lamellae or lamellae stacks (Dionísio et al., 2005). Since the segmental relaxation constrained in the rigid amorphous region thus the dielectric strength is similar even though the orientation is increased. The rigid amorphous regions constrained by the presence of crystalline region; thus, they have a restricted mobility until the surrounding crystals is relaxed. Thus, we may certainly assume that the relaxation occurs primarily in the amorphous region and that the crystalline region contributes the remaining strength.

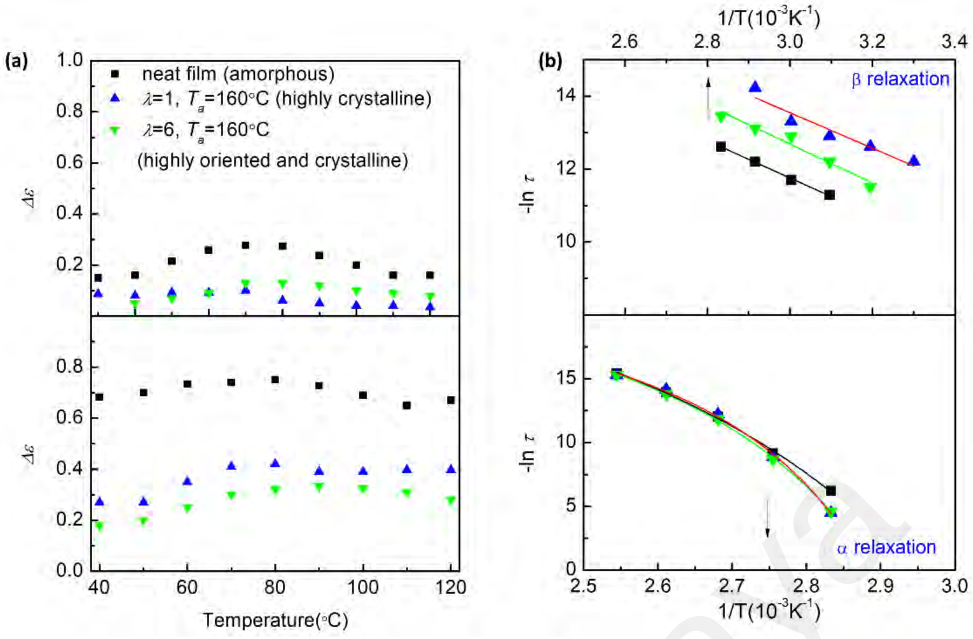

Figure 4.10: (a) Dielectric strength as a function of temperature for *α*- and *β*-relaxation. (b) Arrhenius plots for the *α*- and *β*-relaxation.

The temperature dependence of the relaxation times is shown in Figure 4.10(b). The α-constrained relaxation process exhibits the usual curvature of cooperative processes using the Vogel-Fulcher-Tammann (VFT) equation (refer to Eq. 4.40 below)

$$\tau = \tau_0 e^{\frac{B}{T} - T_0} \tag{4.40}$$

where τ_0 is the pre-exponential factor, B is an activation parameter, and T_0 is the Vogel temperature at which the main-chain is virtually frozen.

In contrary, the β-relaxation showing Arrhenius behaviour described by equation below

$$\tau = \tau_0 e^{E_A kT} \tag{4.41}$$

where $E_A$is the activation energy and k is the Boltzmann constant.

The fitted parameters are displayed in Table 4.3 where τ_o is a pre-exponential factor, B is an activation parameter, and T_f is a so-called Vogel temperature at which the main-chain is virtually frozen. The *B* and T_f value of annealed samples is slightly higher compared to the amorphous films. This is the classical behaviour of macromolecules with the Van der Walls (intermolecular) or hydrogen bonds interactions between the chains (Crétois et al., 2013; Elsawy et al., 2016) and ascribed to the decrease of chain mobility in the vicinity of the crystalline phase. The activation energy of the β-relaxation increases significantly as the crystallinity and orientation increase in the PLLA samples. The activation energy arises from two sources: intra- and intermolecular interactions. Intramolecular interaction most likely unaffected by bulk extension and orientation meanwhile the intermolecular interaction is dependent on the separation distance of atoms and group of atoms on separate molecules (Bernstein & Bhattacharya, 2021). Thus, the intermolecular interaction is be expected to vary with the degree of orientation as the interaction is weaker compared to the intramolecular interaction.

Table 4.3: Parameters of the VFT and Arrhenius equation

Relaxations	Fitted and calculated parameters	Neat film (amorphous)	Annealed sample (high X_c)	T_a =160 °C & λ=6 (oriented crystalline film)
α	$-\ln t_0$ (s)	27.9	24.6	26.7
	B (K)	900	921	926
	T_f(K)	307.4	319.8	313.1
β-sub glass	E_a (kJ/mol)	18.3	40.5	44.5

4.5 Piezoelectric relaxation

By fitting the LE mode equation with the HN function for the λ=6, T_a =160 °C) film, the value of coupling coefficient, k, compliance, s can be obtained from the fitting procedure. The coupling coefficient, k is obtained from

$$k^2 = 1 - \frac{\varepsilon^S}{\varepsilon^T} \tag{4.51}$$

where $\varepsilon^S$is the permittivity at constant strain and ε^Tpermittivity at constant stress.

By inserting the obtained value k and s into Eq. 2.61, the piezoelectric constant, d_{14} and e_{14} can be calculated. Figure 4.11 shows the complex quantity of piezoelectric constant, d_{14}, and e_{14}, elastic constant, c_{44}^*, coupling coefficient, k, compliance, s and dielectric constant, ε for the drawn PLLA ($\lambda = 6$) in the temperature range of 25 °C to 140 °C. The coupling coefficient decrease when temperature increased and a relaxation process could be observed at 100 °C. As shown in Eq. 4.51, the value of k is the ratio of permittivity at constant strain and permittivity at constant stress. Therefore, the changes in k can be observed by decrease of the resonance peak in the dielectric spectra as temperature increased as shown in Figure 4.12. At a higher temperature, k seems to be very small because the resonance peak coincides with the dielectric relaxation. The ε' shows an increase with increasing temperature due to the segmental motion that occur in rigid amorphous region as discussed earlier.

An increase in temperature increases the d_{14}' value and a relaxation process is observed around 110 °C. In contrast, e_{14}' decreases steeply (~70 %) from room temperature up to about 140 °C. Corresponding to the changes in e_{14}', the imaginary e_{14}'' shows a maximum at ~100 °C leading in the dispersion regions. Meanwhile, elastic constant, c_{44}' shows a similar trend as e_{14}, decreasing ~60 % with increasing temperature. Comparatively, the d_{14}' value increases only ~30 % with increasing temperature. By assuming that the dielectric relaxation occurs in the amorphous phase and the piezoelectric relaxation occurs in the crystalline phase, the above results suggests that the crystalline and amorphous regions are connected almost in series. The reason is that when the stress is applied along the draw direction, the stress is homogenous in the crystalline and non-crystalline phases thus d_{14}' is not affected as much as compared to the e'_{14}. However, the relaxation or softening in the amorphous region (non-crystalline phase) results in the reduction of crystalline strain led to the large decrease in e_{14} as the temperature increases. It is also worth noting that a slight increase in d_{14} suggesting the existence of some parallel components in the system and this will be discussed further in the following section.

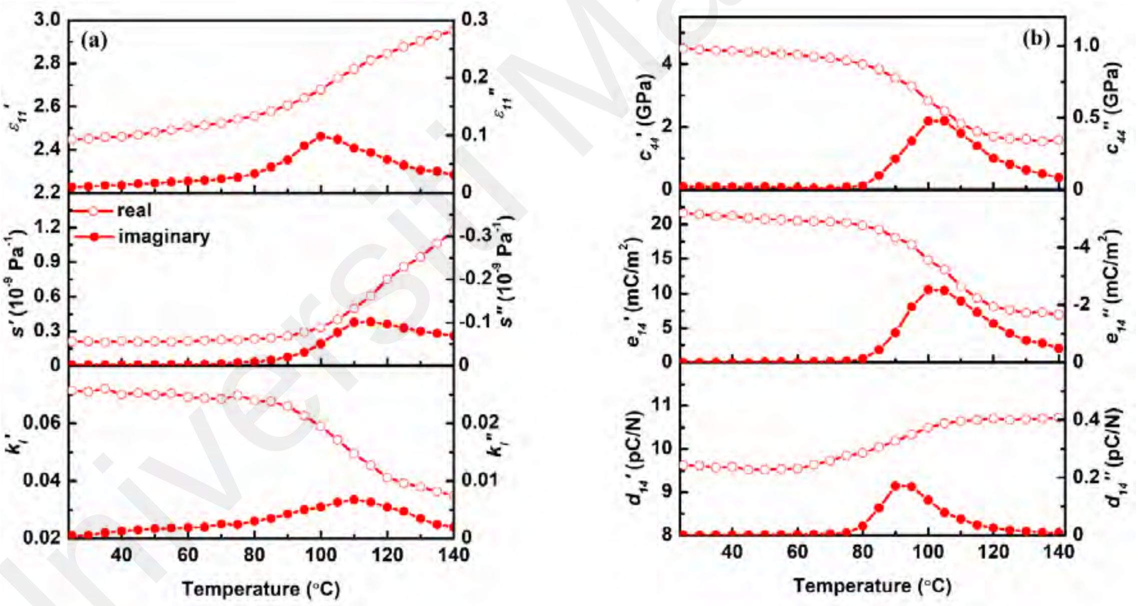

Figure 4.11: Temperature dependence of the (a) coupling coefficient, *k*, compliance, *s* and the dielectric modulus, *ε* at 100 kHz for the oriented PLLA film. and the (b) piezoelectric constant d_{14} and e_{14} and elastic constant, *c*

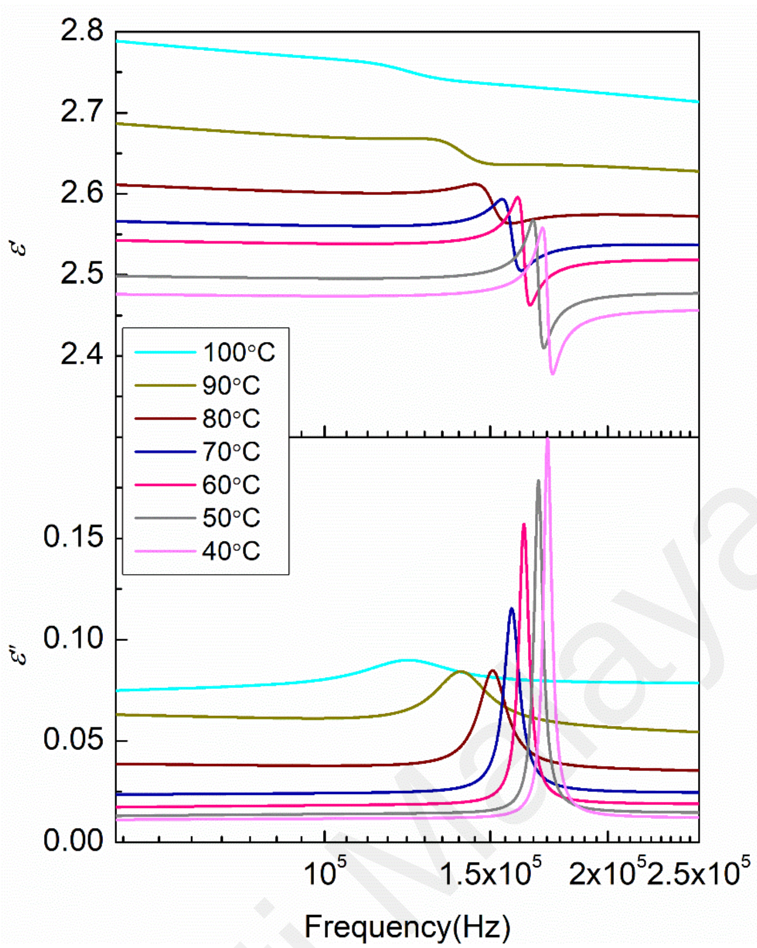

Figure 4.12: The changes in the resonance peaks as the temperature increased from 40 °C to 100 °C is illustrated in the figure.

To study the relationship between amorphous and crystalline region in piezoelectric relaxation, three element model composed of three springs was used (Takeo Furukawa & Fukada, 1976). The elastic three element model is shown in Figure 4.13 where the amorphous region is divided into two components, one in parallel (G_1) and the other in series (G_3) with the crystalline region (G_2). We denote the spring constant as G and variables appearing in this model are the force, F and the deformation, Δl analogous to stress, T and strain S, respectively. The spring constant of spring 1, 2, and 3 are denoted as G_1, G_2, and G_3, respectively.

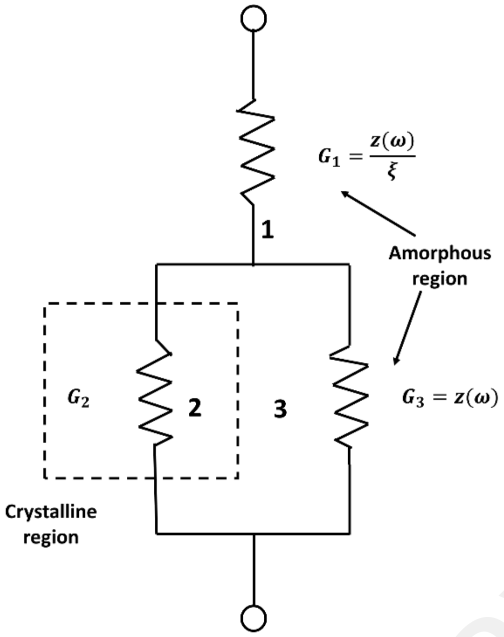

Figure 4.13: Three-spring model consisting of piezoelectric crystalline spring G_2 surrounded by noncrystalline relaxational springs connected in series G_1 and parallel G_3 to G_1.

Spring 2 correspond to crystalline region and spring 1 and 3 correspond to the series and parallel component of amorphous region, respectively. The spring constant G as a whole is then given as

$$G = \frac{G_1(G_2+G_3)}{G_1+G_2+G_3} \tag{4.52}$$

We assume the spring 2 is piezoelectric and nonrelaxing while spring 1 and 3 are nonpiezoelectric and relaxing. The local force in spring 2, F_2 normalized by the applied force, F is

$$L_F \equiv \frac{F_2}{F} = \frac{G_2}{G_2+G_3} \cong L_T \tag{4.53}$$

The local deformation Δl_2, in spring 2 normalized by the applied deformation, Δl, thus

$$L_{\Delta l} \equiv \frac{\Delta l_2}{\Delta l} = \frac{G_1}{G_1+G_2+G_3} \cong L_S \tag{4.54}$$

The variable L is referred to as local field coefficients because they express the local fields in element 2 normalized to the three-element model by the applied field. For the sake of simplicity, we ignored the local electric field in this calculation because the dielectric relaxation strength, $\{\epsilon(0) - \epsilon(\infty)\}/\epsilon(0)$, is less than the elastic relaxation strength, $\{c(\infty) - c(0)\}/c(\infty)$. Furthermore, the dielectric constants of amorphous and crystalline regions are nearly identical ($\varepsilon_1 \approx \varepsilon_2$). The piezoelectric *d*-constant is proportional to L_T, whereas the piezoelectric *e*-constant is proportional to L_S, respectively.

Since G_1 and G_3 are relaxing and are complex values, they can be expressed as follows,

$$G_1 = \frac{z(\omega)}{\zeta} \text{ and } G_3 = z(\omega) \tag{4.55}$$

where $z(\omega)$ is a complex quantity, and ζ is a real number which express the ratio of G_3/G_1. If we assume $z(\omega)$ is a Debye-type single relaxation function, we have

$$z(\omega) = \frac{z(0) + i\omega\tau_z z(\infty)}{1 + i\omega\tau_z}, \qquad (0 \leq \omega \leq \infty) \tag{4.56}$$

where τ_z is the relaxation time, $z(0)$ is the equilibrium value ($\omega = 0$) of $z(\omega)$ and $z(\infty)$ is the instantaneous value ($\omega = \infty$).

Because our piezoelectric constants (see Figure 4.11) are measured in temperature rather than relaxation time, the τ_z was transformed in terms of temperature using the Vogel-Fulcher-Tamman (VFT) equation given below:

$$\tau_z = \tau_0 \exp\left(\frac{B}{T - T_f}\right) \tag{4.57}$$

where τ_0 is the pre-exponential factor, B is an activation parameter, and T_f is the Vogel temperature at which the main chain is virtually frozen.

The complex quantity of G is fitted with the elastic constant, c_{44} using IGOR software. The experimental c_{44} and fitted curve of complex G is shown in Figure 4.14 (a). The c_{44} that been obtained before fit with the complex quantity of G. The value of L_s and L_T also obtained from the fitting and shown in Figure 4.14(b).

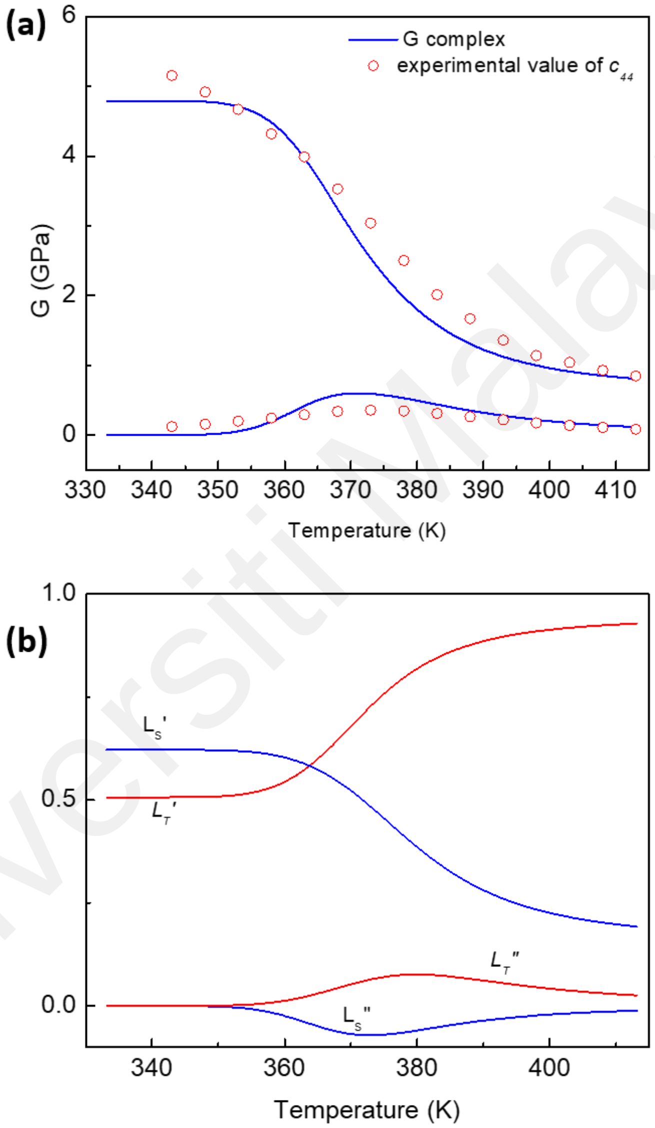

Figure 4.14: (a) The calculated G complex from three element model with the c_{44} and (b) the calculated L_s and L_T.

We determined the spring constant of each spring so that G equaled to the elastic constant, c_{44}, L_F and $L_{\Delta l}$ reproduced the same temperature dependence of d_{14} and e_{14}, respectively. Figure 4.15 illustrates the experimental and fitted temperature spectra for elastic and piezoelectric relaxations. Excellent agreement was obtained using the following best fit parameters

$$G_2 = 4 \times 10^9 \mathrm{N/m} \qquad z(\infty) = 4 \times 10^9 \mathrm{N/m}$$

$$\beta = 0.52 \qquad z(0) = 2 \times 10^8 \mathrm{N/m}$$

$$\zeta = 0.08$$

From these results, we find that marked decrease of e_{14} with temperature is attributed to large series component G_1 and slight increase of d_{14} is attributed to small parallel component G_3 whose ratio being given by ζ=0.08. We can conclude that the structure depicted in Fig. 4.13 is the most basic comparable structure for describing the binary behavior of piezoelectric relaxation in PLLA.

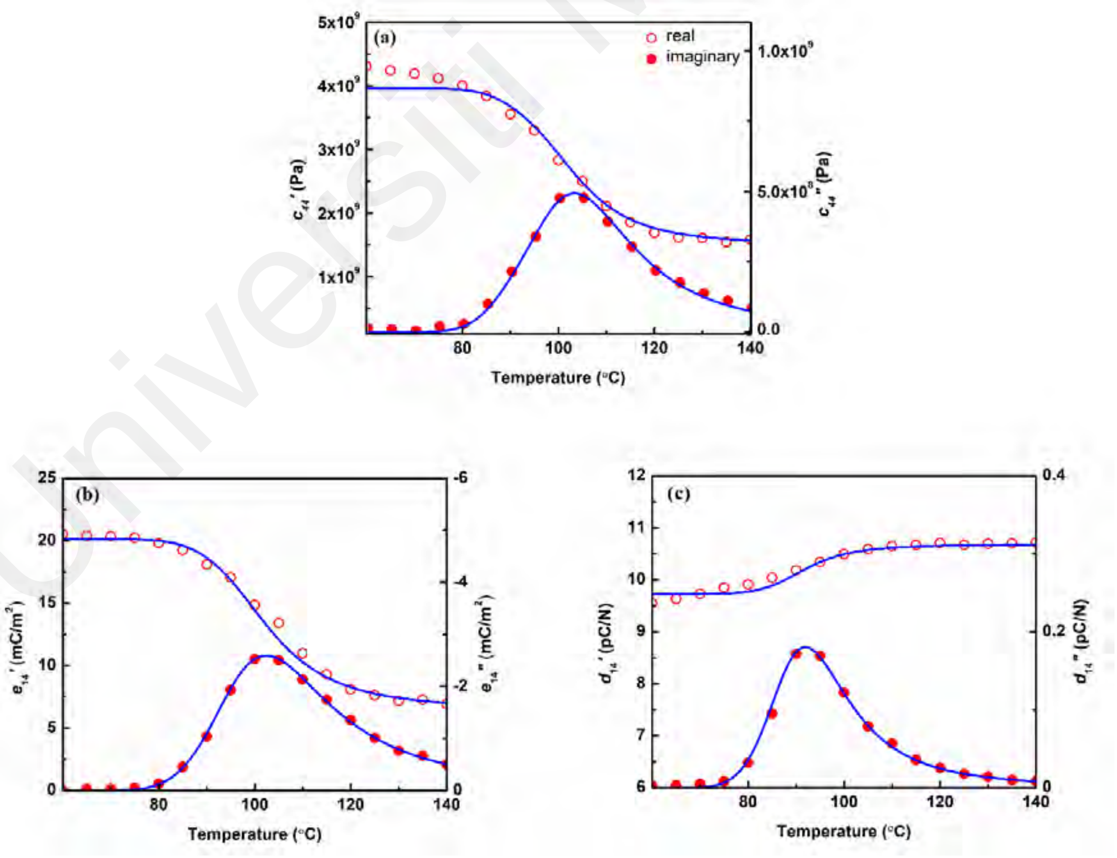

Figure 4.15: The observed experimental results of (a) c_{44}, (b) e_{14} and (c) d_{14} were fitted using a three-element model (the experimental points are the red circles while the fitted curves are the blue lines).

4.6 The effect of crystallinity and chain orientation on the piezoelectric constants of PLLA

This section will examine the relationship between crystallinity index X_c and the orientation factor F_c with the piezoelectric constants of PLLA samples. Previously, Lovell et al. (2011) have shown that X_c and F_c have decoupling effects on the shear piezoelectricity of PLLA, albeit they were only able to achieve $X_c*F_c = 0.05$. In this work, we successfully generated samples with $X_c = 0.8$ and $F_c = 0.9$, yielding an X_c*F_c value of 0.7. We will discuss this in further detail. The piezoelectric constant, e_{14} and d_{14} of PLLA film with different X_c and F_c has been measured at room temperature. Figure 4.16 shows the relationship between crystallinity and orientation factor of the samples. We found that as the orientation factor is raised, the crystallinity increases. This is because the samples were annealed at high temperatures (80 to 160 °C) after they were oriented. Consequently, annealing assisted in the increase of the crystallinity in the oriented samples.

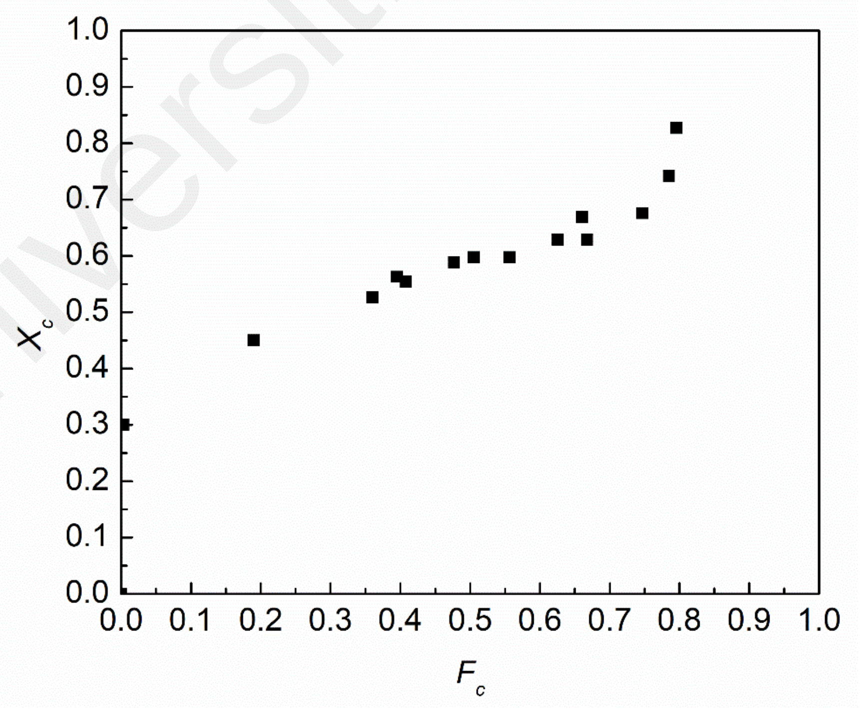

Figure 4.16: Crystallinity, X_c as a function of the orientation, *Fc* for PLLA films.

Shear piezoelectricity was zero in undrawn samples with high crystallinity, which was congruent with the symmetry consideration. Figure 4.17 illustrates the relationship between the e_{14}, d_{14} and c_{44} with X_c*F_c of PLLA samples at room temperature. The low drawing ratio films had lower piezoelectric constants; e_{14} ~4 mC/m^2 and d_{14}~3 pC/N and as the orientation increased, the piezoelectric constants increased. Overall, the piezoelectric constants range from 4 - 23 mC/m^2 and 3 - 9 pC/N depending on the drawing ratios, indicating that uniaxial expansion can have a considerable effect on the PLLA's shear piezoelectricity. The e_{14} is linearly proportional to the product of X_c*F_c. The correlation between c_{44} and X_c*F_c, on the other hand, is also linear. In contrast, d_{14} is not proportional to X_c*F_c but exhibits slight saturation.

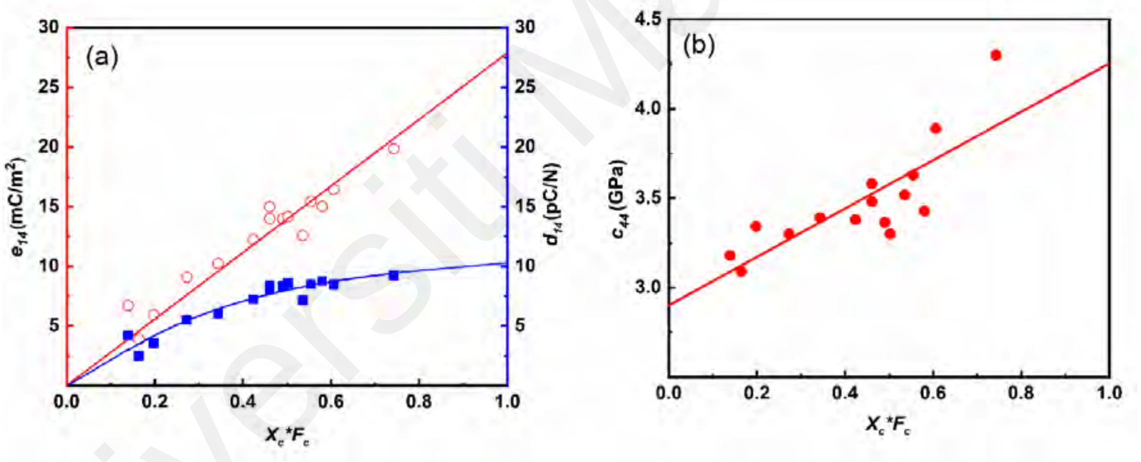

Figure 4.17: Dependence of (a) e_{14} and d_{14} and the (b) c_{44} on the product of X_c*F_c of PLLA samples at room temperature, respectively.

Uniaxially drawn PLLA film consists of oriented crystallites surrounded by noncrystalline molecules. Its piezoelectricity is given by the orientation average of the piezoelectric tensor components of crystallites. It was shown that the piezoelectric stress constant e_{14} is proportional to the F_c with respect to the angle χ between crystalline direction and uniaxial orientation (see the schematic diagram shown in Figure 4.18) and the average of the shear piezoelectric constants of the crystals, e_{14}^{c} and e_{25}^{c} is shown below: (Fukada, 1984; Takeo Furukawa & Fukada, 1976)

$$e_{14} = -e_{25} = X_c F_c \frac{(e_{14}^{c} - e_{25}^{c})}{2} \tag{4.60}$$

In general, the piezoelectric constants of a composite system consisting of piezoelectric crystalline phase dispersed in nonpiezoelectric noncrystalline phase are affected by the difference of dielectric and elastic constant of the respective phases through local field coefficients. When the strain S is applied, it generates the local strain S_c in the piezoelectric phase according to the local strain coefficient $L_S = (S_c/S)$. The local strain S_c generates local piezoelectric polarization P_c according to $e_c = (P_c/S_c)$. The local polarization P_c is observed as the polarization of two-phase system under the condition of short-circuit condition. The ratio of the observed polarization to the local polarization is proven to be given by the local field coefficient $(P_c/S_c)_{E=0} = X_c(E_c/E) = X_c L_E$. As a result, one obtains (Takeo Furukawa & Fukada, 1976),

$$e_{14} = X_c L_E L_S F_c \frac{e_{14}^{c} - e_{25}^{c}}{2} = X_c L_E L_S F_c e_c \tag{4.61}$$

The piezoelectric strain constant d_{14} is given in a similar manner by replacing L_S to the local stress coefficient $L_T = (T_c/T)$.

$$d_{14} = X_c L_E L_T F_c \frac{d_{14}^{c} - d_{25}^{c}}{2} = X_c L_E L_T F_c d_c \tag{4.62}$$

Since

$$d_{14} = e_{14}/c_{44} \tag{4.63}$$

thus

$$\frac{e_{14}}{d_{14}} = c_{44} = \frac{L_S}{L_T}\frac{e_c}{d_c} = \frac{L_S}{L_T} c_c \tag{4.64}$$

where the subscript c refers to crystallites.

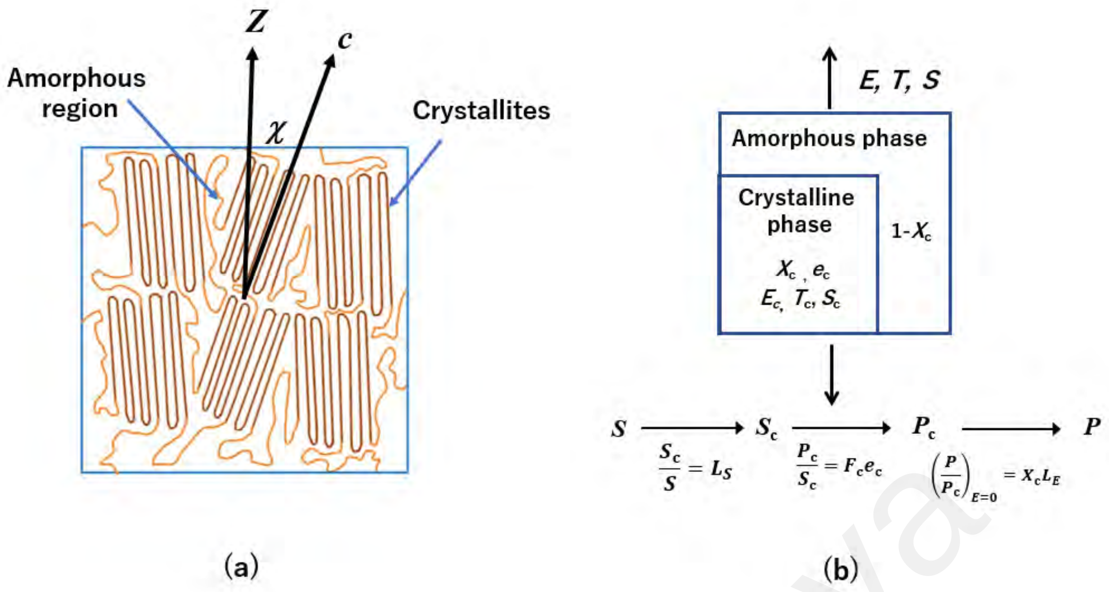

Figure 4.18: Schematic diagram of the (a) drawn semicrystalline polymer consisting of oriented crystallites embedded in amorphous regions (b) parallel-series model expressing oriented semicrystalline polymer consisting of oriented crystallites embedded in amorphous regions.

Figure 4.5 (section 4.2.2) shows that F_c increases dramatically as the annealing temperature rises for λ=3. Drawing has an impact on both the orientation and the value of X_c for a sample annealed at a specific temperature. Furthermore, the quantitative results reveal that when the annealing temperature rises, so does the X_c (Figure 4.4(e)), which is in conformity with the natural expectation.

In this study, drawing was performed at 80 °C which is above T_g and crystallization progresses when the samples are kept at for 1 hour at 80 to 160 °C. We also found that high drawing ratio and high annealing temperature just before melting lead to higher crystallinity due to the thermal agitation. Drawing causes crystals that have previously crystallized to become oriented. The surrounding amorphous molecules made it difficult for the original crystal to entirely orient in the draw direction. Annealing induces the surrounding amorphous molecules to join the orientated original crystals, resulting in an increase in X_c and F_c.

According to the general theory of the face shear piezoelectricity for a two-phase system consisting of piezoelectric crystalline phase surrounded by nonpiezoelectric noncrystalline phase, e_{14} is related to the average of the crystalline piezoelectricity e^c through the product X_c*F_c and the local field coefficient of stress L_T and electric field L_E as given by Eq. (4.61). The local field coefficients reflect the differences of the elastic and dielectric constants between piezoelectric and nonpiezoelectric phases. Since room temperature is far below T_g = 60 ºC the crystalline and noncrystalline phases are with similar elastic and dielectric constants that make L_T and L_E close to unity. Therefore, the linear relationship between e_{14} and X_c*F_c is consistent with Eq. (4.61). As a result, we obtain e^c =27 mC/m^2 that is the average of $e_{14}{}^c$ and $-e_{25}{}^c$ of PLLA crystal. On the other hand, d_{14} is nearly proportional to X_c*F_c, but tends to saturate at high X_c*F_c. This result can be related to the increase in c_{44} and the decrease in L_T. However, full understanding needs further efforts because of marked anisotropy of the fourth rank tensor components of crystalline elasticity.

4.7 Summary

The dielectric and piezoelectric properties of PLLA films have been studied. Our results indicate that the orientation and crystalline content of the PLLA have a strong influence on the piezoelectric properties of the samples. The PLLA film with the highest percentage of crystallinity and orientation factor exhibits the highest piezoelectric constant. The dielectric spectrum revealed two relaxations, i.e., α and β, which are due to segmental motion along the chain backbone and relaxation caused by local twisting motion of the main chains, respectively. The temperature dispersions of e_{14}, d_{14} and c_{44} were reproduced using an equivalent three-spring model consisting of a crystalline piezoelectric spring connected by series and parallel non-crystalline relaxational springs based on the temperature-frequency reduction rule and the VFT-type dielectric relaxation time. The findings revealed key information on the ratio of noncrystalline phases connected in series and parallel to the oriented crystalline phase.

CHAPTER 5: CONCLUSIONS

The relationship between crystallinity, orientation, and shear piezoelectricity of PLLA samples were studied by fabricating the PLLA samples via a dual drawing/annealing technique. In this study we show that PLLA's shear piezoelectricity correlated with the sample's crystallinity and orientation and the product of each of these factors.

A series of PLLA films with well-controlled crystallinity and chain orientation were prepared by drawing and annealing at various drawing ratios and temperatures. By comparing the crystallinity using WAXS and DSC, both results indicated that the X_c increases with the orientation and annealing temperatures. Another important parameter that affects the shear piezoelectric is the orientation factor, F_c which increased simultaneously with the draw ratio and annealing temperature. The results indicate that the chain is well oriented parallel to the draw direction.

The dielectric, elastic and piezoelectric constants of these samples were measured by means of piezoelectric resonance spectroscopy. From our results we conclude that:

(i) The piezoelectric constant, e_{14} was proportional to X_c*F_c that allowed us to evaluate the value of e_{14} of a perfect PLLA crystal which is ~27 mC/m^2. The d_{14}, on the other hand, is not proportional to X_c*F_c but demonstrates saturation while c_{44} increases linearly with X_c*F_c due to X_c and stiffer effective crystalline c_{44}.

(ii) Two distinct dielectric relaxations; namely α-relaxation and sub-glass β-relaxation were observed in the highly oriented and semicrystalline PLLA films.

(iii) Due to segmental motion, the piezoelectric relaxation of e_{14} decreases significantly and d_{14} increases marginally (micro-Brownian motion of non-crystalline segments). This is described by a two-phase model in which crystallites are surrounded by parallel and series non-crystalline regions.

(iv) The decrease of e_{14} with increasing temperature is due to the softening of the non-crystalline phase which causes a decrease of strain in the crystalline phase.

(v) In contrast, the retardation of d_{14} is due to the softening in the non-crystalline region caused by the stress concentration in a parallel crystalline phase.

(vi) The experimental results indicate that the highly crystalline and well-oriented PLLA samples contain a combination of a small amount of parallel and a higher fraction of series non-crystalline phases. The observed temperature dependency of e_{14} and d_{14} can be reproduced by the equivalent model.

Our study suggests that the fabrication of PLLA film for shear piezoelectric applications should focus on generating larger degrees of orientation while heat treating the samples at high temperatures. This process will inevitably lead to an increase in the crystallinity. In nutshell, for a given polymer system, a perfect crystal with maximal crystallinity and orientation will yield the most shear piezoelectricity. While shear piezoelectricity was discovered to be generated by aligned crystalline and amorphous phases, a balance between the relative fractions of each region must be found to ensure the materials' longevity. Only enhanced levels of orientation should be used in optimal shear sensor production, which will also result in a higher crystalline content. This method yields significant shear piezoelectric constants for maximum shear sensing capabilities while retaining adequate degrees of mechanical ductility for processing and application considerations.

We would also like to extend this work by preparing a lower crystallinity and highly oriented samples to study their effects on the piezoelectric constant. Currently our results only concentrated at the mid-range of crystallinity and orientation factor. In addition, analyzing the effect of poling (high electric field application) on dipole alignment will be important.

REFERENCES

Ahmed, J., & Varshney, S. K. (2011). Polylactides—Chemistry, Properties and Green Packaging Technology: A Review. *International Journal of Food Properties, 14*(1), 37-58.

Alegria, A., & Colmenero, J. (2016). Dielectric relaxation of polymers: segmental dynamics under structural constraints. *Soft Matter, 12*(37), 7709-7725.

Alemán, C., Lotz, B., & Puiggali, J. (2001). Crystal Structure of the α-Form of Poly(l-lactide). *Macromolecules, 34*(14), 4795-4801.

Ando, M., Kawamura, H., Kageyama, K., & Tajitsu, Y. (2012). Film Sensor Device Fabricated by a Piezoelectric Poly(L-lactic acid) Film. *Japanese Journal of Applied Physics, 51(9S1)*, Article#09LD14.

Arnau, A., & Soares, D. (2008). Fundamentals of Piezoelectricity. In A. A. Vives (Ed.), *Piezoelectric Transducers and Applications* (pp. 1-38). Berlin, Heidelberg: Springer Berlin Heidelberg.

Auras, R., Harte, B., & Selke, S. (2004). An Overview of Polylactides as Packaging Materials. *Macromolecular Bioscience, 4*(9), 835-864.

Barkhad, M. S., Abu-Jdayil, B., Mourad, A. H. I., & Iqbal, M. Z. (2020). Thermal Insulation and Mechanical Properties of Polylactic Acid (PLA) at Different Processing Conditions. *Polymers, 12*(9), 2091.

Bassett, D. C., & Vaughan, A. S. (1985). On the lamellar morphology of melt-crystallized isotactic polystyrene. *Polymer, 26*(5), 717-725.

Bauer, S., & Bauer, F. (2008). Piezoelectric Polymers and Their Applications. In *Piezoelectricity: Evolution and Future of a Technology* (pp. 157-177). Berlin, Heidelberg: Springer Berlin Heidelberg.

Bernstein, E. R., & Bhattacharya, A. (2021). 6 - Exploring intra- and intermolecular interactions between non-covalently bound species through investigations of clusters: past, present, and future. In E. R. Bernstein (Ed.), *Intra- and Intermolecular Interactions Between Non-covalently Bonded Species* (pp. 189-234): Elsevier.

Brás, A. R., Malik, P., Dionísio, M., & Mano, J. F. (2008). Influence of Crystallinity in Molecular Motions of Poly(l-lactic acid) Investigated by Dielectric Relaxation Spectroscopy. *Macromolecules, 41*(17), 6419-6430.

Brás, A. R., Viciosa, M. T., Wang, Y., Dionísio, M., & Mano, J. F. (2006). Crystallization of Poly(l-lactic acid) Probed with Dielectric Relaxation Spectroscopy. *Macromolecules, 39*(19), 6513-6520.

Carothers, W. H., Dorough, G. L., & Natta, F. J. v. (1932). STUDIES OF POLYMERIZATION AND RING FORMATION. X. THE REVERSIBLE

POLYMERIZATION OF SIX-MEMBERED CYCLIC ESTERS. *Journal of the American Chemical Society, 54*(2), 761-772.

Cartier, L., Okihara, T., Ikada, Y., Tsuji, H., Puiggali, J., & Lotz, B. (2000). Epitaxial crystallization and crystalline polymorphism of polylactides. *Polymer, 41*(25), 8909-8919.

Cartier, L., Okihara, T., Ikada, Y., Tsuji, H., Puiggalí, J., & Lotz, B. (2000). Epitaxial crystallization and crystalline polymorphism of polylactides. *Polymer, 41*, 8909-8919.

Coburn, J. C., & Boyd, R. H. (1986). Dielectric relaxation in poly(ethylene terephthalate). *Macromolecules, 19*(8), 2238-2245.

Crétois, R., Delbreilh, L., Dargent, E., Follain, N., Lebrun, L., & Saiter, J. M. (2013). Dielectric relaxations in polyhydroxyalkanoates/organoclay nanocomposites. *European Polymer Journal, 49*(11), 3434-3444.

Curie, J., & Curie, P. *Développement par compression de l'électricité polaire dans les cristaux hémièdres à faces inclinées*.

de Oca, H. M., & Ward, I. M. (2007). Structure and mechanical properties of poly(L-lactic acid) crystals and fibers. *Journal of Polymer Science Part B: Polymer Physics, 45*(8), 892-902.

De Santis, P., & Kovacs, A. J. (1968). Molecular conformation of poly(S-lactic acid). *Biopolymers, 6*(3), 299-306.

Dillon, B., Doran, P., Fuenmayor, E., Healy, A. V., Gately, N. M., Major, I., & Lyons, J. G. (2019). Influence of Annealing and Biaxial Expansion on the Properties of Poly(l-Lactic Acid) Medical Tubing. *Polymers, 11*(7), Article#1172.

Dionísio, M., Viciosa, M. T., Wang, Y., & Mano, J. F. (2005). Glass Transition Dynamics of Poly(L-lactic acid) during Isothermal Crystallisation Monitored by Real-Time Dielectric Relaxation Spectroscopy Measurements. *Macromolecular Rapid Communications, 26*(17), 1423-1427.

Eling, B., Gogolewski, S., & Pennings, A. J. (1982). Biodegradable materials of poly(l-lactic acid): 1. Melt-spun and solution-spun fibres. *Polymer, 23*(11), 1587-1593.

Elsawy, M. A., Saad, G. R., & Sayed, A. M. (2016). Mechanical, thermal, and dielectric properties of poly(lactic acid)/chitosan nanocomposites. *Polymer Engineering & Science, 56*(9), 987-994.

Fukada, E. (1968). Piezoelectricity as a fundamental property of wood. *Wood Science and Technology, 2*(4), 299-307.

Fukada, E. (1984). Piezoelectricity of natural biomaterials. *Ferroelectrics, 60*(1), 285-296.

Fukada, E. (1995). Piezoelectricity of biopolymers. *Biorheology, 32*(6), 593-609.

Fukada, E. (1998). New Piezoelectric Polymers. *Japanese Journal of Applied Physics, 37*, 2775-2780.

Fukada, E. (2000). History and recent progress in piezoelectric polymers. *IEEE Transactions on Ultrasonics, Ferroelectrics, and Frequency Control, 47*(6), 1277-1290.

Fukada, E., & Ando, Y. (1986). Piezoelectric properties of poly-β-hydroxybutyrate and copolymers of β-hydroxybutyrate and β-hydroxyvalerate. *International Journal of Biological Macromolecules, 8*(6), 361-366.

Furukawa, T. (1989). Piezoelectricity and pyroelectricity in polymers. *IEEE Transactions on Electrical Insulation, 24*(3), 375-394.

Furukawa, T., & Fukada, E. (1976). Piezoelectric relaxation in poly(γ-benzyl-glutamate). *Journal of Polymer Science: Polymer Physics Edition, 14*(11), 1979-2010.

Gotro, J. (2014). Thermoset Characterization Part 1: Introduction to DSC.

Guerin, S., Tofail, S. A. M., & Thompson, D. (2019). Organic piezoelectric materials: milestones and potential. *NPG Asia Materials, 11*(1), Article#10.

Heeley, E. L., Billimoria, K., Parsons, N., Figiel, Ł., Keating, E. M., Cafolla, C. T., . . . Hughes, D. J. (2020). In-situ uniaxial drawing of poly-L-lactic acid (PLLA): Following the crystalline morphology development using time-resolved SAXS/WAXS. *Polymer, 193*, Article#122353.

Hemminger, W., & Sarge, S. M. (1998). Chapter 1 - Definitions, Nomenclature, Terms and Literature. In M. E. Brown (Ed.), *Handbook of Thermal Analysis and Calorimetry* (Vol. 1, pp. 1-73): Elsevier Science B.V.

Hikosaka, S., Ishikawa, H., & Ohki, Y. (2011). Effects of crystallinity on dielectric properties of poly(L-lactide). *Electronics and Communications in Japan, 94*(7), 1-8.

Hoogsteen, W., Postema, A. R., Pennings, A. J., Ten Brinke, G., & Zugenmaier, P. (1990). Crystal structure, conformation and morphology of solution-spun poly(L-lactide) fibers. *Macromolecules, 23*(2), 634-642.

Kanchanasopa, M., & Runt, J. (2004). Broadband Dielectric Investigation of Amorphous and Semicrystalline l-Lactide/meso-Lactide Copolymers. *Macromolecules, 37*(3), 863-871.

Katzir, S. (2012). Who knew piezoelectricity? Rutherford and Langevin on submarine detection and the invention of sonar. *Notes and Records of the Royal Society, 66*(2), 141-157.

Kawai, T., Rahman, N., Matsuba, G., Nishida, K., Kanaya, T., Nakano, M., . . . Matsuda, M. (2007). Crystallization and Melting Behavior of Poly (l-lactic Acid). *Macromolecules, 40*(26), 9463-9469.

Kobayashi, J., Asahi, T., Ichiki, M., Oikawa, A., Suzuki, H., Watanabe, T., . . . Shikinami, Y. (1995). Structural and optical properties of poly lactic acids. *Journal of Applied Physics, 77*(7), 2957-2973.

Kong, Y., & Hay, J. N. (2002). The measurement of the crystallinity of polymers by DSC. *Polymer, 43*(14), 3873-3878.

Kong, Y., & Hay, J. N. (2003). The enthalpy of fusion and degree of crystallinity of polymers as measured by DSC. *European Polymer Journal, 39*(8), 1721-1727.

Kortaberria, G., Marieta, C., Jimeno, A., Arruti, P., & Mondragon, I. (2007). Crystallization of poly(L-lactid acid) monitored by dielectric relaxation spectroscopy and atomic force microscopy. *Journal of Microscopy, 224*, 277-289.

Krigbaum, W. R., & Roe, R. J. (1964). Crystallite Orientation in Materials Having Fiber Texture. II. A Study of Strained Samples of Crosslinked Polyethylene. *The Journal of Chemical Physics, 41*(3), 737-748.

Lovell, C. S., Fitz-Gerald, J. M., & Park, C. (2011). Decoupling the effects of crystallinity and orientation on the shear piezoelectricity of polylactic acid. *Journal of Polymer Science Part B: Polymer Physics, 49*(21), 1555-1562.

Lowe, C. E. (1952a). United States Patent No. US2668162A.

Lowe, C. E. (1952b). United States Patent No. US2668162A.

Mellinger, A. (2003). Dielectric resonance spectroscopy: a versatile tool in the quest for better piezoelectric polymers. *IEEE Transactions on Dielectrics and Electrical Insulation, 10*(5), 842-861.

Mierzwa, M., Floudas, G., Dorgan, J., Knauss, D., & Wegner, J. (2002). Local and global dynamics of polylactides.: A dielectric spectroscopy study. *Journal of Non-Crystalline Solids*, 296-303.

Mijović, J., & Sy, J.-W. (2002). Molecular Dynamics during Crystallization of Poly(l-lactic acid) As Studied by Broad-Band Dielectric Relaxation Spectroscopy. *Macromolecules, 35*(16), 6370-6376.

Montes de Oca, H., & Ward, I. (2007). Structure and mechanical properties of poly(L-lactic acid) crystals and fibers. *Journal of Polymer Science Part B: Polymer Physics, 45*, 892-902.

Nishi, M., Kano, K.,Takahashi, Yoshiyuki,Furukawa, T. (1999, 1999/12/1). *Piezoelectric resonance in uniaxially oriented films of chiral polymers.* Paper presented at the 10th International Symposium on Electrets (ISE 10).

Ounaies, Z., Young, J. A., & Harrison, J. S. (1999). An Overview of the Piezoelectric Phenomenon in Amorphous Polymers. In *Field Responsive Polymers* (Vol. 726, pp. 88-103): American Chemical Society.

Pan, P., Kai, W., Zhu, B., Dong, T., & Inoue, Y. (2007). Polymorphous Crystallization and Multiple Melting Behavior of Poly(l-lactide): Molecular Weight Dependence. *Macromolecules, 40*(19), 6898-6905.

Ren, J. (2011). Biodegradable Poly(Lactic Acid): Synthesis, Modification, Processing and Applications.

Ren, J., & Adachi, K. (2003). Dielectric Relaxation in Blends of Amorphous Poly(dl-lactic acid) and Semicrystalline Poly(l-lactic acid). *Macromolecules, 36*(14), 5180-5186.

Ru, J.-F., Yang, S.-G., Zhou, D., Yin, H.-M., Lei, J., & Li, Z.-M. (2016). Dominant β-Form of Poly(l-lactic acid) Obtained Directly from Melt under Shear and Pressure Fields. *Macromolecules, 49*(10), 3826-3837.

Rudnik, E. (2008). Biodegradability testing of compostable polymer materials. In Rudnik, E. (Ed.), *Compostable Polymer Materials* (pp.112-166). Amsterdam (NL):Elsevier.

Sasaki, S., & Asakura, T. (2003). Helix Distortion and Crystal Structure of the α-Form of Poly(l-lactide). *Macromolecules, 36*(22), 8385-8390.

Schönhals, A., & Kremer, F. (2003). Analysis of dielectric spectra. In *Broadband dielectric spectroscopy* (pp. 59-98): Springer.

Shin, D.-M., Hong, S. W., & Hwang, Y.-H. (2020). Recent Advances in Organic Piezoelectric Biomaterials for Energy and Biomedical Applications. *Nanomaterials, 10*(1), 123.

Sosnowski, S. (2001). Poly(l-lactide) microspheres with controlled crystallinity. *Polymer, 42*(2), 637-643.

Sultana, A., Ghosh, S. K., Sencadas, V., Zheng, T., Higgins, M. J., Middya, T. R., & Mandal, D. (2017). Human skin interactive self-powered wearable piezoelectric bio-e-skin by electrospun poly-l-lactic acid nanofibers for non-invasive physiological signal monitoring. *Journal of Materials Chemistry B, 5*(35), 7352-7359.

Tajitsu, Y. (2007, 27-31 May 2007). *Piezoelectricity of Chiral Polymeric Fiber and its Application in Biomedical Engineering.* Paper presented at the 2007 Sixteenth IEEE International Symposium on the Applications of Ferroelectrics.

Tajitsu, Y. (2008). Piezoelectricity of chiral polymeric fiber and its application in biomedical engineering. *IEEE Trans Ultrason Ferroelectr Freq Control, 55*(5), 1000-1008.

Tajitsu, Y. (2010). Basic study on controlling piezoelectric motion of chiral polymeric fiber. *IEEE Transactions on Dielectrics and Electrical Insulation, 17*(4), 1050-1055.

Tajitsu, Y. (2016). Smart piezoelectric fabric and its application to control of humanoid robot. *Ferroelectrics, 499*(1), 36-46.

Tajitsu, Y., Kawai, S., Kanesaki, M., Date, M., & Fukada, E. (2004). Microactuators with Piezoelectric Polylactic Acid Fibers—Toward the Realization of Tweezers for Biological Cells. *Ferroelectrics, 304*(1), 195-200.

Tanaka, M., & Young, R. J. (2006). Molecular Orientation Distributions in Uniaxially Oriented Poly(l-lactic acid) Films Determined by Polarized Raman Spectroscopy. *Macromolecules, 39*(9), 3312-3321.

Tanimoto, K., Saihara, S., Adachi, Y., Harada, Y., Shiomi, Y., & Tajitsu, Y. (2015). Shear piezoelectricity of optically active polysuccinimides. *Japanese Journal of Applied Physics, 54*, 10NF02.

Tichý*, J., Erhart, J., Kittinger*, E., & Přívratská, J. (2010). Piezoelectric Properties. In *Fundamentals of Piezoelectric Sensorics: Mechanical, Dielectric, and Thermodynamical Properties of Piezoelectric Materials* (pp. 69-100). Berlin, Heidelberg: Springer Berlin Heidelberg.

Uchino, K. (2017). The Development of Piezoelectric Materials and the New Perspective. In (pp. 1-92).

Vink, E. T. H., & Davies, S. (2015). Life Cycle Inventory and Impact Assessment Data for 2014 Ingeo™ Polylactide Production. *Industrial Biotechnology, 11*(3), 167-180.

Wang, Y., Funari, S. S., & Mano, J. F. (2006). Influence of Semicrystalline Morphology on the Glass Transition of Poly(L-lactic acid). *Macromolecular Chemistry and Physics, 207*(14), 1262-1271.

Wübbenhorst, M., & Turnhout, J. (2012). Analysis of complex dielectric spectra. I. One-dimensional derivative techniques and three-dimensional modelling. *Journal of Non-Crystalline Solids, 305*, 40-49.

Yoshida, T., Imoto, K., Tahara, K., Naka, K., Uehara, Y., Kataoka, S., . . . Tajitsu, Y. (2010). Piezoelectricity of Poly(L-lactic Acid) Composite Film with Stereocomplex of Poly(L-lactide) and Poly(D-lactide). *Japanese Journal of Applied Physics, 49*(9), 09MC11-09MC11.

Zhang, J., Tsuji, H., Noda, I., & Ozaki, Y. (2004). Structural Changes and Crystallization Dynamics of Poly(l-lactide) during the Cold-Crystallization Process Investigated by Infrared and Two-Dimensional Infrared Correlation Spectroscopy. *Macromolecules, 37*(17), 6433-6439.